HEALTH AND MEDICINE

# An inverse-breathing encapsulation system for cell delivery

**Long-Hai Wang[1], Alexander Ulrich Ernst[1], James Arthur Flanders[2], Wanjun Liu[1], Xi Wang[1], Ashim K. Datta[1], Boris Epel[3], Mrignayani Kotecha[4], Klearchos K. Papas[5], Minglin Ma[1]***



**Cell encapsulation represents a promising therapeutic strategy for many hormone-deficient diseases such as type 1 diabetes (T1D). However, adequate oxygenation of the encapsulated cells remains a challenge, especially in the poorly oxygenated subcutaneous site. Here, we present an encapsulation system that generates oxygen ($O_2$) for the cells from their own waste product, carbon dioxide ($CO_2$), in a self-regulated (i.e., "inverse breathing") way. We leveraged a gas-solid ($CO_2$–lithium peroxide) reaction that was completely separated from the aqueous cellular environment by a gas permeable membrane. $O_2$ measurements and imaging validated $CO_2$-responsive $O_2$ release, which improved cell survival in hypoxic conditions. Simulation-guided optimization yielded a device that restored normoglycemia of immunocompetent diabetic mice for over 3 months. Furthermore, functional islets were observed in scaled-up device implants in minipigs retrieved after 2 months. This inverse breathing device provides a potential system to support long-term cell function in the clinically attractive subcutaneous site.**

## INTRODUCTION

The transplantation of immunoprotected therapeutic-secreting cells has promised to provide a compliance- and immunosuppression-free cell replacement therapy for many hormone-deficient diseases and endocrine disorders such as type 1 diabetes (T1D) (*1*–*3*). T1D affects millions of people worldwide and currently does not have a cure (*4*). Cell encapsulation technology intends to regulate blood glucose (BG) levels autonomously and prevent immune destruction of transplanted donor islets or stem cell–derived insulin-producing cells from the host by the use of a semipermeable material that prevents graft interaction with immune effector cells.

It has been well documented that a critical constraint of cell replacement therapy is insufficient oxygen ($O_2$) supply (*5*, *6*). Pancreatic islets—cell clusters comprising glucose-sensing, insulin-secreting β cells and other secretory cells—are densely vascularized in their native state due to the high $O_2$ demand of insulin secretion (*7*). However, they are dissociated from arterial blood following isolation and encapsulation. This limits $O_2$ delivery to slow passive diffusion from extra-arterial sources in the transplantation site, which are comparatively low (*5*, *8*–*10*). In particular, the partial pressure of $O_2$ ($pO_2$) experienced by a native β cell in the pancreas is roughly 40 to 60 mmHg (*8*), whereas it is likely below 25 mmHg for cells in a transplanted islet (*8*, *11*). Hydrogel encapsulation further exacerbates this issue by increasing the $O_2$ diffusion distances to the cell clusters (*12*), and the deposition of a fibrotic capsule around the graft during the foreign body reaction (*13*) often adds yet another mass transfer resistance limiting cellular $O_2$ availability. The subcutaneous (SC) space is one of the most clinically desirable transplantation sites due to its minimally invasive accessibility. However, it is particularly $O_2$ limited and produces high levels of fibrotic deposition following material implantation (*9*, *14*).

$O_2$ limitations affect both islet survival and metabolic function and possibly increase immunogenicity. Steep $pO_2$ gradients within isolated islets restrict $O_2$ flow to the islet core. This central hypoxia has deleterious consequences: At a $pO_2$ of ~8 mmHg, β cell insulin secretion is substantially arrested (*15*), and at levels below ~0.08 mmHg, islet cells undergo programmed and unprogrammed cell death (*15*, *16*). These apoptotic and necrotic cells release danger-associated molecular patterns to which the host mounts an immune response, increasing the recruitment of immune cells to the graft (*17*, *18*). This phenomenon may aggravate $O_2$ limitations by increasing $O_2$ depletion at the graft-host interface, thereby reducing the amount available for the encapsulated cells (*19*). Hypoxia notably impairs the metabolic responsiveness of encapsulated islets and may also precipitate a positive feedback loop of worsening graft oxygenation and immunogenicity.

One of the most straightforward ways to address inadequate oxygenation in cell therapies is to directly inject $O_2$ into the encapsulation device. Animal studies (*20*–*23*) and a preliminary human trial (*24*) clearly showed the benefit of $O_2$ supplementation despite the requirement of tedious daily injections. In situ chemical $O_2$ generation is an emerging biomaterial strategy to supply $O_2$ without human intervention (*25*). Several inorganic peroxides spontaneously release $O_2$ or hydrogen peroxide (which decomposes to yield $O_2$) in aqueous environments. For example, sodium percarbonate [$(Na_2CO_3)_2{\cdot}1.5H_2O_2$] and calcium peroxide ($CaO_2$) provided short-term (1 to 10 days) $O_2$ supply following their incorporation in degradable scaffolds (*26*, *27*). Pedraza *et al.* (*28*) extended the duration of $O_2$ generation in these constructs to approximately 1 month by embedding $CaO_2$ particulates within a polydimethylsiloxane (PDMS) disk, which slowed the production rate by introducing a diffusional barrier between the water and the reactive particulates. This construct reduced hypoxic effects in encapsulated β cells transplanted intraperitoneally in mice, demonstrating that enhanced oxygenation improved graft outcomes and reduced the expression of immunostimulatory factors (*29*). However, water is not an optimal reactant for in vivo $O_2$ generation because its transport is difficult to regulate.

In this work, we developed a novel $O_2$-generating system regulated by carbon dioxide ($CO_2$), effectively decoupling $O_2$ generation

[1]Biological and Environmental Engineering, Cornell University, Ithaca, NY 14853, USA. [2]Department of Clinical Sciences, Cornell University, Ithaca, NY 14853, USA. [3]Department of Radiation and Cellular Oncology, The University of Chicago, Chicago, IL 60637, USA. [4]O2M Technologies LLC, Chicago, IL 60612, USA. [5]Department of Surgery, University of Arizona, Tucson, AZ 85724, USA.
*Corresponding author. Email: mm826@cornell.edu

from cellular needs (e.g., water) and instead to a waste product of cellular respiration (Fig. 1). In this "inverse-breathing" system, $CO_2$ released from respiring islets and cells in the host tissue (Eq. 1) is recycled into $O_2$ by lithium peroxide ($Li_2O_2$), thereby comprising a self-sustaining system (Eq. 2 and Fig. 1A)

$$\text{Glucose} + 6\,O_2 \rightarrow 6\,CO_2 + 6\,H_2O + \text{ATP} \quad (1)$$

$$2\,Li_2O_2 + 2\,CO_2 \rightarrow 2\,Li_2CO_3 + O_2 \quad (2)$$

In human tissues, $CO_2$ is ubiquitously available at a partial pressure ($pCO_2$) regulated to approximately 40 mmHg (*30*). In addition, when exposed to high glucose levels such as after a meal, β cell $CO_2$ production and $O_2$ demand are increased in tandem (*31*). Accordingly, $CO_2$ is both a ubiquitous and dynamic reactant optimally suited to control $O_2$ delivery to encapsulated cells. By immersing $Li_2O_2$ in a perfluorocarbon (PFC) oil, which has the capacity to dissolve high concentrations of $CO_2$ and $O_2$, and isolating the formulation from the hydrogel-encapsulated cells through a gas-permeable, liquid-impermeable silicone membrane, the self-regulated release of $O_2$ can be achieved without influencing the aqueous cellular environment. Given the high $O_2$ content of $Li_2O_2$ (2.1-fold higher than $CaO_2$ considering commercial purities), and the fact that the $O_2$ generation and cellular encapsulation compartments are separated, $O_2$ release can last for months with one implantation and may be further extended by increasing the loading capacity or through refilling.

Here, we present proof-of-concept studies involving the design, modeling, testing, and optimization of the Inverse Breathing Encapsulation Device (iBED) for potential T1D treatment. We show that a simple inverse-breathing construct produced $O_2$ in a $CO_2$-responsive and sustainable manner, mitigating hypoxia in proximally encapsulated cells during incubation in a low $O_2$ environment. Using a first-generation iBED prototype, we demonstrated notably improved survival and function of rat islets in immunocompetent, streptozotocin (STZ)–induced diabetic mice within the poorly oxygenated SC site. A computational model, validated by in vitro $O_2$ measurements and $pO_2$ distribution mapping, guided the optimization of the iBED system, yielding a device that achieved diabetes reversal for over 3 months in the SC rat-to-mouse model. These optimized designs featured a terminal tank containing the PFC-immersed $Li_2O_2$ formulation connected to a hollow silicone tube coated with a cell encapsulation hydrogel layer. Last, a scaled-up device was developed for large animal testing. Unexpectedly, rat islet survival was observed after retrieval at 1 and 2 months in an SC rat-to-pig xenotransplantation, despite the wide species gap and challenging SC environment. The iBED design presented here could overcome several outstanding challenges in oxygenating encapsulated cells and represents considerable progress in the use of translatable long-term $O_2$-supplementing technologies for cell replacement therapies.

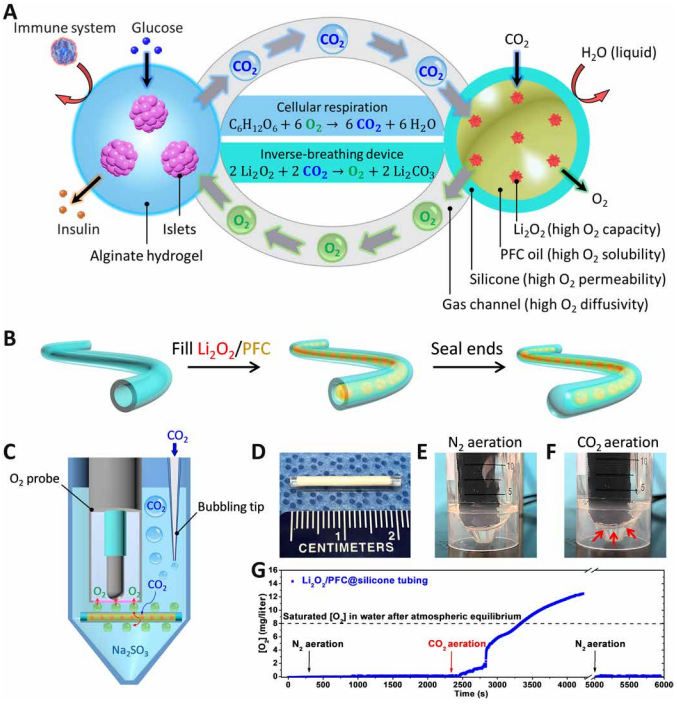


**Fig. 1. An inverse-breathing system for encapsulated cells.** (**A**) A schematic representation of the inverse-breathing system: Islets were encapsulated in a semipermeable alginate hydrogel that permitted the transport of nutrients and the delivery of insulin but prevented the infiltration of immune effector cells; $CO_2$ released from the cells was rapidly transported in the gas phase to PFC-encapsulated $Li_2O_2$ particulates, contained within a gas-permeable, liquid-impermeable silicone membrane, whereby $CO_2$ was recycled into $O_2$. (**B**) Fabrication steps for a test construct. (**C**) A schematic representing the $CO_2$-responsive $O_2$ generation confirmation test: A construct was submerged in $Na_2SO_3$-deoxygenating buffer and aerated with $CO_2$; the $CO_2$ diffused through the silicone tubing and reacted with the encapsulated $Li_2O_2$, leading to $O_2$ bubble generation and accumulation on the construct's surface; the $O_2$ bubbles attached to the bottom of the $O_2$ probe, diffused through the gas permeable membrane of the $O_2$ probe, and were detected by the electrode. (**D**) A digital image of a test construct. (**E** and **F**) Digital images of the test assembly during (E) $N_2$ aeration and (F) $CO_2$ aeration (arrows indicate generated $O_2$ bubbles). (**G**) $O_2$ production over time measured by the submerged $O_2$ probe near the device (arrows indicate aeration phase start times). Photo credits: (D to F) Long-Hai Wang, Cornell University.

## RESULTS

### A $CO_2$-regulated $O_2$ delivery system for encapsulated cells

A simple construct was developed to demonstrate the ability of silicone membrane-isolated $Li_2O_2$ to recycle $CO_2$ into $O_2$. Biocompatible [USP (United States Pharmacopeia) Class VI] silicone tubing [2 cm in length, inner diameter (i.d.) of ~1.47 mm, and outer diameter (o.d.) of ~1.96 mm) was filled with 20% (w/w) $Li_2O_2$ particulates immersed in PFC oil ($Li_2O_2$/PFC) and sealed at the ends with curable PDMS resin (Fig. 1B). Silicone-based materials were desirable because of their high-gas (e.g., $O_2$ and $CO_2$) permeability (*32*), good corrosion resistance (*33*), and ability to physically isolate the particulate suspension. PFC oil was an optimal medium for $Li_2O_2$ because of its high $O_2$ and $CO_2$ solubility and its water-resistant properties (*34*), as the presence of water may unwantedly accelerate the $O_2$-generating reaction (*35*). In concept, $CO_2$ from the encapsulated cells and the surrounding tissues diffuses through the silicone tubing and is recycled into $O_2$ via $Li_2O_2$, which, in turn, diffuses radially to be consumed by the encapsulated cells. To test this concept, the $Li_2O_2$/PFC@silicone construct was submerged in an aqueous solution containing sodium sulfite ($Na_2SO_3$), an $O_2$ scavenging agent used to maintain negligible dissolved $O_2$ levels in the solution, and subjected to three aeration phases: (i) a 100% nitrogen gas ($N_2$) phase, (ii) a

100% $CO_2$ phase, and (iii) a second 100% $N_2$ phase (Fig. 1, C to F). A lithium carbonate ($Li_2CO_3$)/PFC formulation, which is inert to $CO_2$, was used in place of $Li_2O_2$/PFC as a negative control. $O_2$ measurements with a Clark electrode (fig. S1) showed baseline $O_2$ levels (~0 mg/liter) during the first $N_2$ aeration phase (Fig. 1E), a rapid increase from bubbles released from the tubing surface during the $CO_2$ aeration phase (Fig. 1F), and a return to near-zero levels during the second $N_2$ aeration phase after the purging of bubbles formed in the second phase (Fig. 1G). No $O_2$ production was observed in control $Li_2CO_3$/PFC@silicone samples following testing under this aeration regime (fig. S2). In addition, incubation of the $Li_2O_2$/PFC@silicone construct in saline for several weeks did not change the solution pH. These findings validated that the silicone-encapsulated $Li_2O_2$/PFC formulation was $CO_2$-responsive and securely packed.

## Improvement of cell survival during in vitro hypoxic incubation and in vivo

The $Li_2O_2$/PFC@silicone construct was subsequently adapted to support cell encapsulation and investigated in its ability to improve cell viability during hypoxic incubation in vitro (Fig. 2). Here, the surface of the silicone tubing was modified, ensuring robust attachment of the cell-laden hydrogel coating (Fig. 2A). Briefly, a layer of macroporous PDMS was attached to the silicone tubing to increase the surface roughness (fig. S3), and a polydopamine coating was then added to provide hydrophilicity. Alginate (a ~500-μm layer) was chosen for cell encapsulation due to its ease of crosslinking and biocompatibility (*36*).

We tested the ability of the $Li_2O_2$/PFC formulation to enhance cellular $O_2$ supply by incubating this construct in hypoxic conditions. INS-1 cells [alginate (2.5 million cells/ml)] were incorporated into $Li_2O_2$/PFC@silicone constructs and $Li_2CO_3$/PFC@silicone controls and incubated at 1% $O_2$ and 5% $CO_2$. Live/dead staining of samples after 24 hours of hypoxic incubation revealed that only a thin layer of cells near the hydrogel buffer interface survived in the controls (Fig. 2B), whereas most cells in the $Li_2O_2$/PFC@silicone iBED samples were viable (Fig. 2C). The iBED yielded a 2.7-fold improvement in cell viability in comparison to the control device (fig. S4). This study was also performed with rat islets [500 islet equivalent number (IEQ) within 100 μl of alginate]. After 24 hours of hypoxic incubation, pimonidazole (fig. S5) was used to evaluate hypoxia in islets. While a notable accumulation of pimonidazole protein adducts was observed in the control sample islets (Fig. 2D and fig. S6A), only minimal amounts were detected in the $Li_2O_2$/PFC@silicone islets (Fig. 2E and fig. S6B). Furthermore, hematoxylin and eosin (H&E) and insulin/glucagon immunostaining revealed only one to three layers of intact and insulin-positive cells in control islets (Fig. 2F and fig. S7, A to F), whereas virtually all $Li_2O_2$/PFC@silicone islets were intact and positive for insulin throughout and glucagon in peripheral cells (Fig. 2G and fig. S7, G to L). In addition, in core cells of nearly all control islets, pyknosis (shrunken and dark nuclei) was detected (Fig. 2F and fig. S7, A to C), and karyorrhexis (fragmented nuclei) were seen in some larger islets (Fig. 2F and fig. S7, C and F), signs of apoptosis and necrosis (*16*). Specifically, islets in the control devices showed a 1.86-fold reduction of insulin expression due to the noninsulin secretion cells in the hypoxic core and 1.25-fold reduction in 4′,6-diamidino-2-phenylindole (DAPI) content because of the shrunken or fragmented nuclei compared to islets in the iBED devices (fig. S7M). These outcomes indicated that $O_2$ production from $Li_2O_2$/PFC-containing

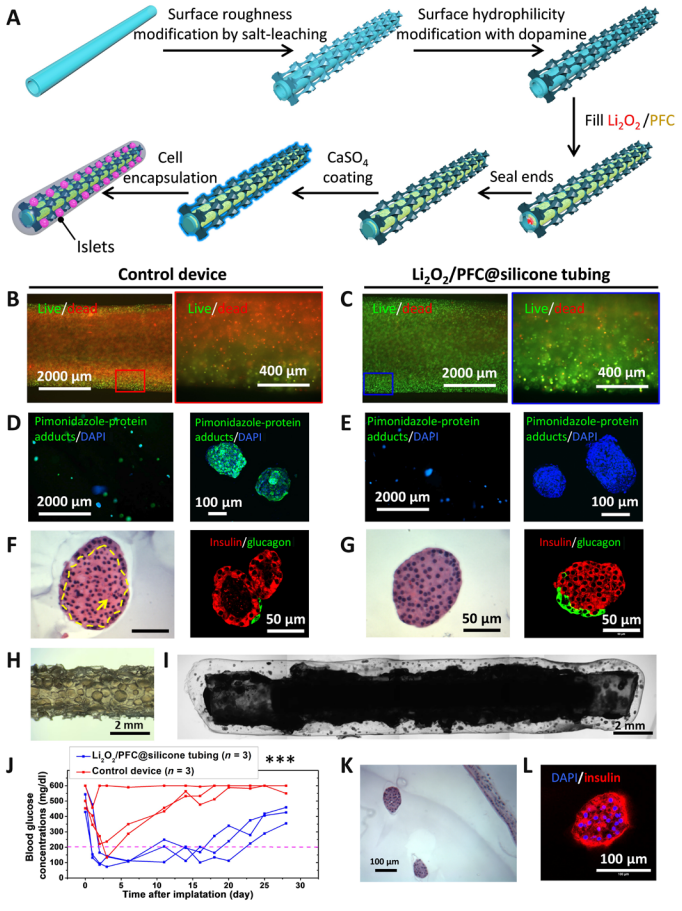


**Fig. 2. Improvement of cell survival during in vitro hypoxic incubation and in vivo.** (**A**) Fabrication of a $Li_2O_2$/PFC@silicone construct. (**B** and **C**) Fluorescent microscopy images of INS-1 cells stained for viability (alive, green; dead, red) following 24-hour culture in 1% $O_2$ and 5% $CO_2$ in (B) $Li_2CO_3$/PFC controls and (C) $Li_2O_2$/PFC-containing constructs. (**D** and **E**) Immunostaining of nuclei (DAPI; blue) and pimonidazole-protein adducts (green) following 24-hour culture in 1% $O_2$, 5% $CO_2$ of islets in (D) $Li_2CO_3$/PFC controls, and (E) $Li_2O_2$/PFC-containing constructs. (**F** and **G**) H&E-stained islets (left) and insulin- (red) and glucagon-immunostained (green) islets (right) after 24-hour hypoxic culture in (F) $Li_2CO_3$/PFC controls (yellow arrow indicates nuclear fragmentation; yellow outline circumscribes pyknotic cells) and (G) $Li_2O_2$/PFC-containing constructs. (**H**) Stereo microscope image of the surface-modified silicone tubing. (**I**) Microscope image of construct with encapsulated rat islets. (**J**) BG readings in $Li_2O_2$/PFC-containing islet encapsulation constructs ($n = 3$) and $Li_2CO_3$/PFC islet encapsulation controls ($n = 3$) over a 4-week transplantation period; $^{***}P < 0.001$. (**K**) H&E and (**L**) nuclei (DAPI, blue) and insulin-stained (red) islets retrieved from $Li_2O_2$/PFC-containing construct.

constructs improved cell survival and function under hypoxic culture conditions.

In vivo outcomes of the $Li_2O_2$/PFC@silicone cell encapsulation construct were explored next. The SC space was selected as the site of implantation for its clinical desirability. Its low $pO_2$ levels, reported to range from <8 to 40 mmHg (*9*, *37*), also provided a challenging hypoxic environment to test the capability of the construct. Rat islets (500 IEQ per transplant) in 100 μl of alginate were incorporated in $Li_2O_2$/PFC@silicone constructs ($n = 3$) and $Li_2CO_3$/PFC@silicone controls ($n = 3$) and transplanted in the dorsolateral SC space of STZ-induced diabetic C57BL6/J mice (Fig. 2, H and I).

BG lowering was observed in control-treated mice for only 1 to 3 days following transplantation, whereas hyperglycemia reversal (<200 mg/dl) was sustained for 16 to 20 days in the group treated with the $Li_2O_2$/PFC@silicone samples (Fig. 2J). H&E staining of retrieved islets from $Li_2O_2$/PFC@silicone samples showed several well-defined islets with no observable signs of hypoxia (Fig. 2K), although a few unhealthy islets were found as well (fig. S8, A and B). In addition, immunostaining revealed insulin-positive cells (Fig. 2L), suggestive of maintained islet function. These studies confirmed that the $Li_2O_2$/PFC formulation, regulated by physiological $CO_2$, could mitigate hypoxia in cell encapsulation devices, providing a foundational proof of concept of the inverse-breathing $O_2$-generating system.

## iBED prototype reverses hyperglycemia in mice

Encouraging results from the proof-of-concept studies prompted the design of a prototype with the intention of prolonging the duration of $O_2$ supply (Fig. 3). A first-generation iBED prototype (iBEDv1) was developed, featuring a three-dimensional (3D) printed terminal $Li_2O_2$/PFC reserve tank to increase the formulation storage capacity (Fig. 3A). A dental resin was used for the printing of the terminal tank, because it is both biocompatible and impermeable to gas, which prevented $O_2$ leakage (Fig. 3B and fig. S9). Briefly, iBEDv1 was fabricated by filling the terminal tank with 20% (w/w) $Li_2O_2$/PFC and attaching it to the $Li_2O_2$/PFC@silicone construct (1.5 cm; fabricated as previously described) at the tank neck via a gas-permeable PDMS adapter (Fig. 3, B to D). The terminal reserve tank increased the $Li_2O_2$/PFC storage capacity, and, likewise, theoretical total $O_2$ output, eightfold, featured a deliberately low surface area of gas exchange at the tank neck and was therefore hypothesized to substantially extend the duration of $O_2$ supply.

Rat islets (500 IEQ per transplant) within 80 μl of alginate were incorporated in iBEDv1 prototypes ($n = 10$) and controls, which did not include the $Li_2O_2$/PFC formulation ($n = 5$). The devices were transplanted in the dorsolateral SC space of STZ-induced diabetic C57BL6/J mice (figs. S10 and S11). Control-treated mice exhibited lowered random BG levels for 1 to 10 days before returning to a hyperglycemic state, whereas 7 of 10 iBEDv1-treated mice exhibited lowered BG levels over 60 days (Fig. 3E). While normoglycemia (<200 mg/dl) was restored for approximately 15 days in 7 of 10 iBEDv1-treated samples, the BG rose steadily to a range between 200 and 300 mg/dl following this initial period. This coincided with the time frame of normal BG restoration for the simple $Li_2O_2$/PFC@silicone construct (Fig. 2J), suggesting a possible drop in efficacy once the particulates within the lumen of the silicone tubing were consumed.

An intraperitoneal glucose tolerance test (IPGTT) was administered at 58 days to three iBEDv1-treated subjects, each of which exhibited moderate glycemia at this stage (Fig. 3F). The BG of the treated group returned to normoglycemia after 120 to 180 min (slightly delayed in comparison to healthy control mice), whereas the BG of the control device-treated mice did not fall below 400 mg/dl during this period. Following retrieval, the hydrogel was stripped from one device for imaging and staining, and the tank/silicone tubing assembly was incubated in saline buffer at 5% $CO_2$ for 3 hours. Bubbles were observed at the tubing surface, suggesting that $O_2$ generation was still active at 60 days (Fig. 3G). Bubbles first appeared on the tubing closer to the tank and gradually formed down the lumen over time, indicating the possible presence of an $O_2$ gradient in $z$ direction of the tubing lumen (fig. S12). According to H&E staining,

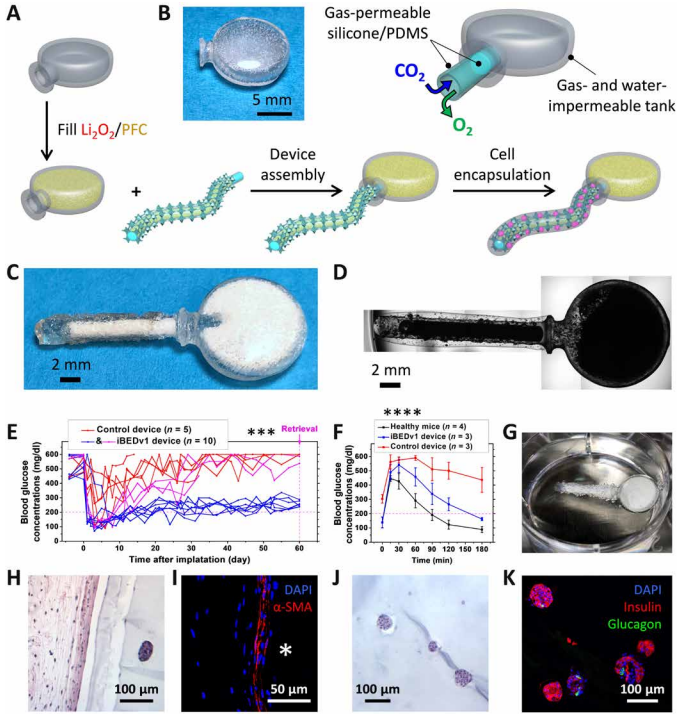


**Fig. 3. iBEDv1 design and diabetes reversal in mice following SC transplantation.** (**A**) Device assembly of iBEDv1. (**B**) Digital image of the 3D printed terminal tank (left) and an annotated schematic (right) showing the direction of gas transfer through the PDMS adapter. (**C**) Digital image of the iBEDv1 device. (**D**) Microscope image of the iBEDv1 device, including the rat islet encapsulation hydrogel. (**E**) BG measurements in C57BL6/J mice following SC transplantation of control devices (red; $n = 5$) and iBEDv1 devices (blue, well-controlled BG; pink, poorly controlled BG; $n = 10$) over 60 days; $^{***}P < 0.001$ (control versus iBEDv1). (**F**) IPGTT test at 58 days; means ± SD, $^{****}P < 0.0001$ (all treatment comparisons). (**G**) Digital image of a retrieved device (stripped of its hydrogel layer) in 5% $CO_2$ buffer, showing bubble formation at the scaffold surface. (**H**) H&E-stained slides after retrieval emphasizing the fibrotic layer adjacent to the device. (**I**) Nuclei (DAPI; blue) and alpha–smooth muscle actin (α-SMA) (red) immunostaining showing the fibrotic layer adjacent to the device surface (the asterisk indicates device). (**J**) H&E, (**K**) nuclei (DAPI; blue), insulin (red), and glucagon (green) immunostaining in islets retrieved from iBEDv1 device. Photo credits: (B to D and G) Long-Hai Wang, Cornell University.

a modest deposition of fibrotic tissue was found adjacent to the hydrogel (Fig. 3H). The fibrotic tissue showed no signs of inflammation, myofibroblasts were identified by α–smooth muscle actin staining (Fig. 3I), and only rare and sporadic T cells were found in CD3 staining (fig. S13B). H&E-stained iBEDv1 islets in animals with moderately controlled BG were observed with preserved morphology (Fig. 3J), and immunostaining revealed several insulin- and glucagon-positive cell clusters (Fig. 3K), although a few unhealthy islets were found far away from the tank, possibly due to limited $O_2$ transport to this region (fig. S13, C and D). Some islets in a retrieved iBEDv1 from a mouse with elevated BG levels (fig. S14) showed necrosis in the mantle of the islet, rather than the core, suggesting that the observed cell death might not be due to hypoxia (fig. S14, D and E). Higher amounts of T cells and macrophages were found in the fibrotic tissue surrounding failed iBEDv1 samples (fig. S14, A to C) in comparison to successful ones. Control islets were largely fragmented, and several were totally necrosed (fig. S15). The promising

results from this study further confirmed the benefit of this $CO_2$-responsive $O_2$ delivery system to encapsulated islets and suggested that the duration of $O_2$ supply could be extended by attaching an additional $Li_2O_2$/PFC reservoir in connection with the device.

## Model-aided design optimization

We next used computational modeling to estimate the impact of design modifications on islet oxygenation (Fig. 4). The iBEDv1 prototype featured a silicone tubing filled with the $Li_2O_2$/PFC formulation. However, the $Li_2O_2$ content within the lumen was only sufficient to produce $O_2$ to support the encapsulated rat islets for ~1 week. We expected that after the $O_2$ content within the lumen was consumed, slow $O_2$ diffusion in the formulation would retard transport between the tank and cells. Our second-generation design (iBEDv2) thus considered the replacement of the $Li_2O_2$/PFC formulation in the lumen with air (by simply not filling it), hypothesizing that this would improve overall $O_2$ delivery, as diffusion in air is roughly 10,000-fold faster than in PFC (*38*, *39*). Expanding the advantage of fast gas-phase $O_2$ diffusion, a hollow channel through port from the lumen into the tank was incorporated to accelerate gas exchange. We also considered decreasing the silicone tubing thickness to reduce the diffusive resistance of $O_2$ over this silicone barrier and increasing its surface area to improve $O_2$ distribution throughout the hydrogel phase. The third-generation design (iBEDv3) featured a quadruple helix of thinner hollow silicone tubing (i.d., ~0.34 mm; o.d., ~0.64 mm). $O_2$ transport was simulated in a finite element model to compare the relative efficacy of these designs in comparison to a control device without $O_2$ supply (Fig. 4, A and B, and figs. S16 and S17).

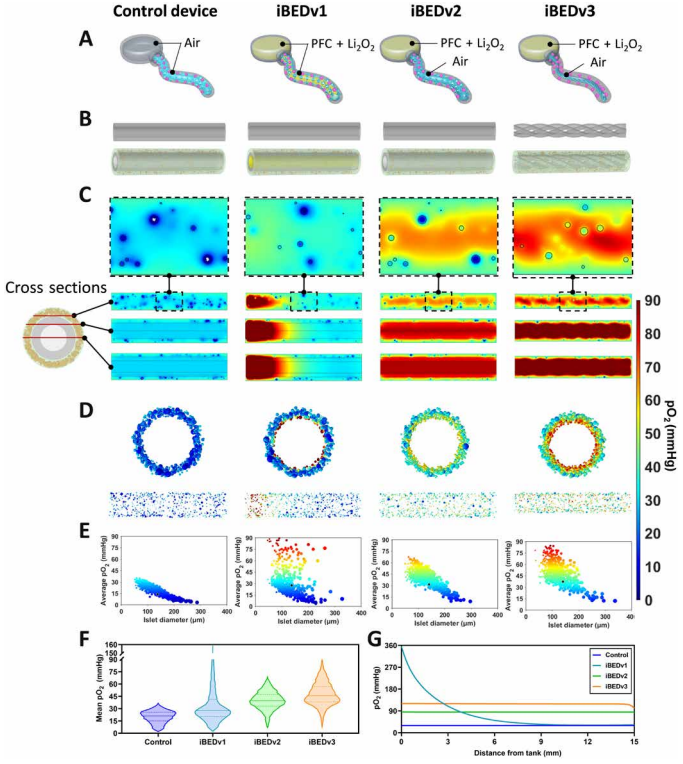


**Fig. 4. Computational model-guided design optimization.** (**A**) Schematics representing design iterations. (**B**) Schematics representing simulated geometry for each design, showing the silicone tubing structures (top) and full geometry (bottom) including the randomly seeded islets (yellow), alginate (green), silicone tubing (gray), and lumen material (white, air; yellow, PFC). (**C**) $pO_2$ distributions in three cross-sections (indicated by the diagram on the left) of each design showing low and uniform $pO_2$ in the control, a gradient of $pO_2$ in the iBEDv1, and high and uniform $pO_2$ in iBEDv2 and iBEDv3. A high magnification image selected from one cross section is also presented (top); white regions represent necrosis. (**D**) Islet surface $pO_2$ distributions from the *xy*- (top) and *yz*- (bottom) perspectives. (**E**) Scatter plots of islet volume-average $pO_2$ versus islet diameter (black circle indicates volume-weighted average islet diameter and $pO_2$; each dot represents one islet). (**F**) Frequency of islet volume-average $pO_2$ in each design, showing high concentration of poorly oxygenated islets in the control and iBEDv1 and a high concentration of well-oxygenated islets in iBEDv2 and iBEDv3; solid lines represent medians, and dashed lines represent first and third quartiles. (**G**) $pO_2$ along a center line of the device.

In general, the iBEDv2 and iBEDv3 designs performed more desirably than the control device and iBEDv1. Cross-sectional surface plots showed a uniformly low $pO_2$ distribution in the control device, as expected, due to the lack of an exogenous $O_2$ supply system (Fig. 4C). A steep $pO_2$ gradient was visualized along the *z* direction in iBEDv1, with $pO_2$ levels resembling that of the control levels by the midpoint of the device. This indicated that the formulation did restrict $O_2$ transfer to regions far away from the tank. The iBEDv2 and iBEDv3 designs, however, displayed high and uniform oxygenation throughout and attributed to the vastly superior gas-phase diffusivity within the tubing lumens. Distributions of $pO_2$ on the islet surfaces further show that only islets near the tank were well oxygenated in iBEDv1, whereas islet oxygenation was independent of tank distance in iBEDv2 and iBEDv3 (Fig. 4D and fig. S18). The volume-average $pO_2$ of each islet was calculated, showing that oxygenation was strongly inversely correlated with islet diameter (Fig. 4E), a result of the high $O_2$ consumption rate of rat islets (*40*). Nonetheless, volume-average islet $pO_2$ fell below 8 mmHg (the threshold necessary for insulin secretion) (*41*) in a large fraction of control and iBEDv1 islets, whereas even the largest iBEDv2 and iBEDv3 islets were above this threshold. Organizing volume-average islet $pO_2$ by frequency showed that most of the islets in the control or iBEDv1 were poorly oxygenated, whereas only a small fraction of poorly oxygenated islets was observed in iBEDv2 and even smaller fraction in iBEDv3 (Fig. 4F). The low frequency of well-oxygenated iBEDv1 islets can be attributed to the fact that those near the tank received substantial $O_2$, whereas those further away did not. The slight advantage of iBEDv3 in comparison to iBEDv2 may be due to the increased surface area and decreased thickness of the silicone tubing, although the slightly smaller alginate diameter may contribute some effect as well. The comparison between each design may be summarized by comparing the $pO_2$ measured along a centerline of the device (Fig. 4G and fig. S19). iBEDv1 centerline $pO_2$ was higher than iBEDv2 or iBEDv3 levels for ~20% of the device length but inferior in the remaining ~80% and virtually no better than the control in 50%. In addition, centerline $pO_2$ was slightly higher in iBEDv3 than in iBEDv2 throughout. Collectively, these results indicated the combined advantages of $O_2$ supply by the inverse-breathing system and rapid gas-phase $O_2$ diffusion in the tubing lumens.

Model results provided several critical insights. Of primary concern was the question of whether the magnitude of $O_2$ generation would contribute a notable benefit. Simulated islet oxygenation showed a substantial improvement in iBED islets in comparison to control levels for all designs. Results also revealed the limitations of filling the silicone tubing lumen with the $Li_2O_2$/PFC formulation

and indicated that the simple adjustment of maintaining a gas phase therein would improve uniformity of $O_2$ delivery. Last, the model suggested that further improvements could be achieved by using thinner silicone tubing in a high surface area configuration. In effect, modeling here enabled the expedient identification of an optimized design.

### $O_2$ distribution mapping using an electron paramagnetic resonance imager

Real-time 3D $pO_2$ distribution mapping was performed to measure $CO_2$-regulated $O_2$ release in the iBEDv3 (Fig. 5 and fig. S20). These measurements were acquired using pulse electron paramagnetic resonance (EPR) $O_2$ imaging (*42*–*44*) via a 25-mT preclinical $O_2$ imager, the JIVA-25 instrument (O2M Technologies LLC, Chicago, IL) (Fig. 5, A and B). Briefly, devices were submerged in 3 ml of solution in a sealed glass test tube with a water-soluble trityl radical molecular probe (1 mM OX063-d24) (Fig. 5C) (*45*). $O_2$-sensitive electron spin-lattice relaxation rates ($R_1$) of the trityl radical in phosphate-buffered saline (PBS; at 1 mM) were measured by JIVA-25 and converted into $pO_2$ according to a calibration curve (Fig. 5D). A gas inlet and a gas outlet were introduced to the sealed glass test tube (fig. S20A) to subject the devices to an aeration regime (fig. S20B): (i) a 100% $N_2$-bubbling phase to deoxygenate the system, (ii) a gas-mixture bubbling phase to equilibrate the system to the desired dissolved gas levels, and (iii) an overhead flow phase, whereby the gas inlet was retracted from the liquid to the space above the sample, and the gas mixture was circulated over the solution to maintain exposure to the supplied gas mixture after equilibration while reducing perturbance of the fluid.

This procedure was first performed with a control device and an iBEDv3 in an aqueous solution using a gas mixture of 5% $CO_2$, 5% $O_2$, and 90% $N_2$. Average $pO_2$ measurements of the whole system (i.e., solution and device) and distribution mapping showed that the control sample rose from ~5 mmHg after deoxygenation to near equilibrium levels ($pO_2$ of ~40 mmHg) for the remainder of the experiment (Fig. 5E). On the other hand, the $pO_2$ in the iBEDv3 sample exceeded equilibrium $pO_2$ rapidly during the overhead flow phase and continued rising even at 20 hours to ~180 mmHg (Fig. 5F), confirming that $O_2$ production in iBEDv3 was responsive to physiological $CO_2$ levels (i.e., $pCO_2$ of ~40 mmHg).

We then repeated this study with the devices submerged in 1% gelatin, which is more viscous than water, and was thus expected to reduce fluid mixing and therefore resolve $pO_2$ gradients in the system. Here, an $O_2$-free gas mixture of 5% $CO_2$ and 95% $N_2$ was used. In the control sample, average $pO_2$ levels trended toward ~0 mmHg after deoxygenation over the duration of the experiment, and $pO_2$ distributions were uniform and low (Fig. 5G). In the iBEDv3 sample, average $pO_2$ reached a steady state of 30 to 40 mmHg after ~2 hours of overhead flow (Fig. 5H and fig. S20C). A clear $pO_2$ gradient was distinguishable at all time points, where $pO_2$ values were highest near the silicone tubing and decreased with distance. At steady state (>2 hours), the $pO_2$ values near the silicone tubing were between 60 and 80 mmHg (Fig. 5H and fig. S20C); they also appeared to be constant with distance from the tank, suggesting uniform oxygenation throughout the silicone tubing lumens, corroborating model predictions. Repeating iBEDv3 measurements in 1% gelatin with a gas mixture of 5% $CO_2$, 5% $O_2$, and 90% $N_2$ showed an average steady-state $pO_2$ of ~80 mmHg, with steady-state $pO_2$ levels near the silicone tubing at ~140 mmHg (fig. S20D). We suspected that, in studies with 1% gelatin, the rise in average sample $pO_2$ did not continue for as long as in studies with water because of poor $CO_2$ penetration from overhead flow; this was supported by measurements showing almost no $O_2$ penetration beyond ~0.5 cm in 1% gelatin at ~22 hours during 5% $O_2$ overhead flow (fig. S20E). Nonetheless, these $pO_2$ distribution studies clearly indicated robust responsiveness to physiological $CO_2$ levels and thorough $O_2$ transport along the silicone tubing of the iBEDv3, supporting its capability to enhance oxygenation in vivo.

### iBEDv3 design enables 3-month diabetes correction in mice via SC implantation

Following $O_2$ mapping, the iBEDv3 was studied in vivo (Fig. 6). The simulation-guided design improvements and additional modifications were implemented in iBEDv3. Two hollow silicone tubes (i.d., ~0.34 mm; o.d., ~0.64 mm) were twisted, folded at the middle, and then sealed at the ends, creating a four-thread twisted structure resembling the simulated quadruple helix (Fig. 6A). This twisted structure was then fit through a larger, short-silicone hollow cylinder (length, ~4 mm; i.d., ~1.47 mm), and fixed into place by filling the larger silicone tubing with PDMS resin and curing. This reduced $O_2$ and $CO_2$ diffusive resistance by allowing gas-phase transport through the adapter in the twisted tubing lumens (Fig. 6, B and C), instead of through the solid-phase PDMS as in iBEDv1 and iBEDv2 (fig. S21A). A liquid perfusion study was performed, confirming that the lumens of the tubing remained hollow after twisting, signaling that gas-phase $O_2$ transport would not be interrupted (Fig. 6, D and E, and movie S1). Thereafter, the adapter was affixed to the terminal tank via PDMS resin (Fig. 6F). Rapid formation of bubbles at the tubing surface following a manual injection of air illustrates the high-gas permeability of the silicone tubing (Fig. 6G and movie S2). Last, islet encapsulation in alginate was performed, yielding the completed device (Fig. 6, H and I). Note that silicone surface roughness modification was not needed, as hydrogel attachment to the twisted structure was sufficiently robust, consistent with other findings from our group (*46*, *47*).

iBEDv3 devices containing $Li_2O_2$/PFC ($n$ = 10) or $Li_2CO_3$/PFC (controls; $n$ = 7), both encapsulating 500 IEQ of rat islets (within 60 μl alginate), were transplanted in the dorsolateral SC space of STZ-induced diabetic C57BL6/J mice. Normoglycemia was achieved in 8 of 10 iBEDv3-treated mice for 92 days, whereas all control subjects reverted to hyperglycemia quickly after transplantation (Fig. 6J). The engraftment percent of the iBEDv3 was maintained at 80% over 3 months, which was significantly better than that of the iBEDv1 with the engraftment dropping to 30% at 2 months (fig. S21G). BG levels in the iBEDv3-treated animals returned to hyperglycemic levels after device retrieval, indicating that the device was responsible for the observed BG regulation. In an IPGTT at 90 days, iBEDv3-treated animals showed lowered BG levels after 90 min, similar to the healthy control mice, whereas control-treated mice did not exhibit lowered BG levels similar to the diabetic control mice (Fig. 6K). Again, the iBEDv3 showed significantly better function than the iBEDv1, showing a faster glucose clearance during the IPGTT (fig. S21H). In addition, iBEDv3 devices retrieved at 92 days were glucose-responsive (stimulation index, 5.6 ± 1.3) in a static glucose-stimulated insulin secretion (GSIS) assay (Fig. 6L). Micro–computed tomography (micro-CT) imaging of a device implanted in a mouse showed that the hollow lumen structure was maintained (Fig. 6M and fig. S22).

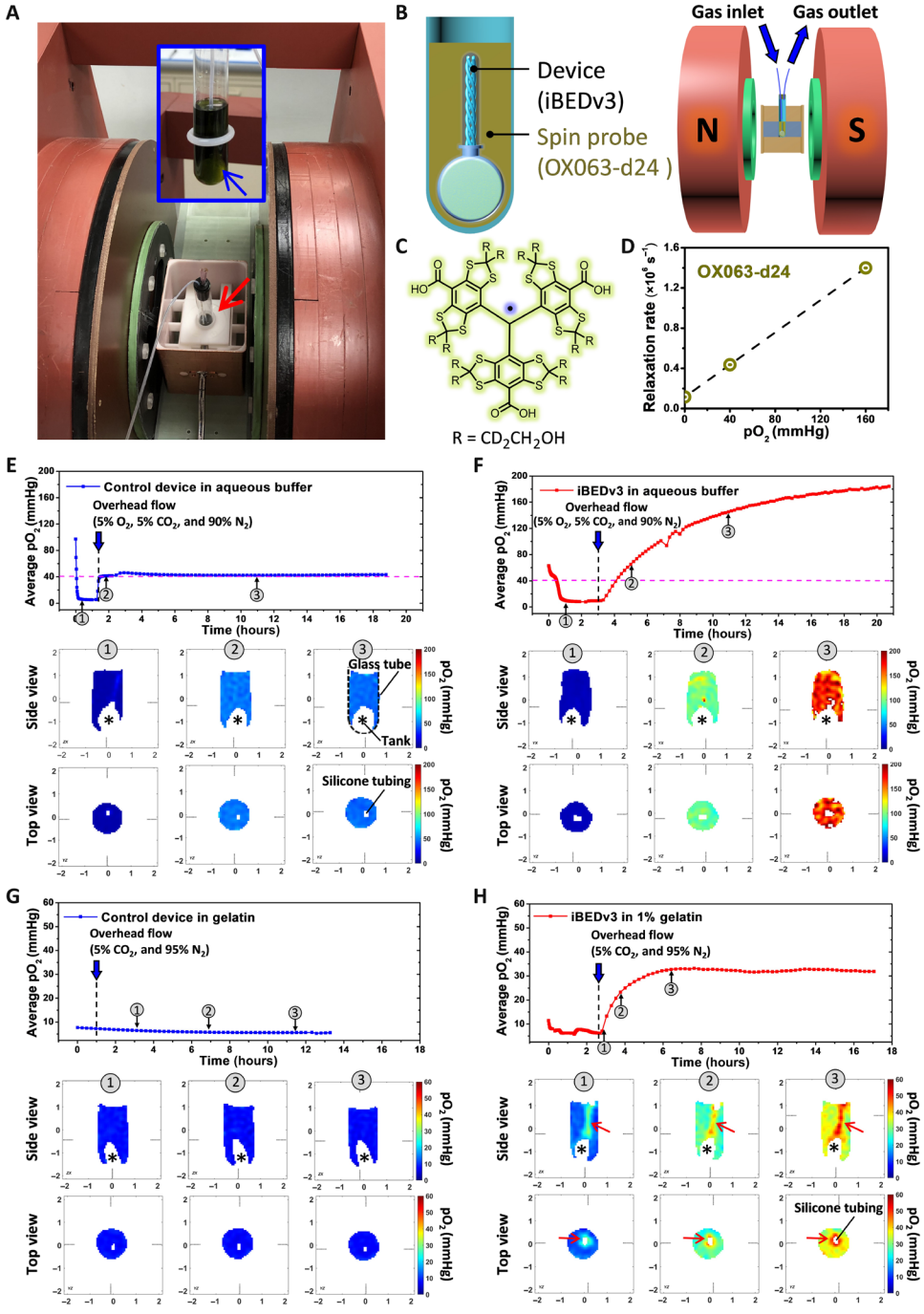


**Fig. 5. EPR $O_2$ imaging.** (**A**) A digital image of the JIVA-25 instrument (red arrow indicates sample location). Inset figure shows a digital image of an iBEDv3 submerged in OX063-d24 aqueous buffer (blue arrow indicates the iBEDv3). (**B**) Schematic representation of the EPR instrument setup. (**C**) Chemical structure of OX063-d24. (**D**) Calibration curve used for obtaining $pO_2$ from relaxation rates of OX063-d24. (**E** to **H**) Average $pO_2$ measurements in the whole system (solution and device) versus time and cross-section $pO_2$ distributions on two planes (side view and top view) at three times (indicated by the arrows in the time series plots). The asterisks indicate the tank located at the bottom of the glass tube, and the hollow empty regions on top view images indicate the silicone tubing of the iBEDv3. (E) A control device sample and (F) an iBEDv3 sample in aqueous buffer subjected to 5% $CO_2$, 5% $O_2$, and 90% $N_2$ (pink dashed line indicates equilibrium $O_2$: $pO_2 = 40$ mmHg, i.e., 5% $O_2$). (G) A control device sample and (H) an iBEDv3 device sample in 1% gelatin subjected to $O_2$-free 5% $CO_2$ and 95% $N_2$. The red arrows indicate the regions of high $pO_2$ around the silicone tubing of the iBEDv3. Photo credit: (A) Mrignayani Kotecha, O2M Technologies LLC.

Following retrieval at 92 days, stereo microscope imaging showed that islets appeared as yellow with maintained smooth and intact morphology at all distances from the terminal tank, suggesting that islet health was preserved (Fig. 6N). Incubation of the device in 5% $CO_2$ buffer resulted in the formation of bubbles at the tubing surface, which indicated that $O_2$ production from the supply tank was maintained at this time point as well (Fig. 6, O and P, and fig. S23). H&E-stained slides and insulin/glucagon immunostaining confirmed

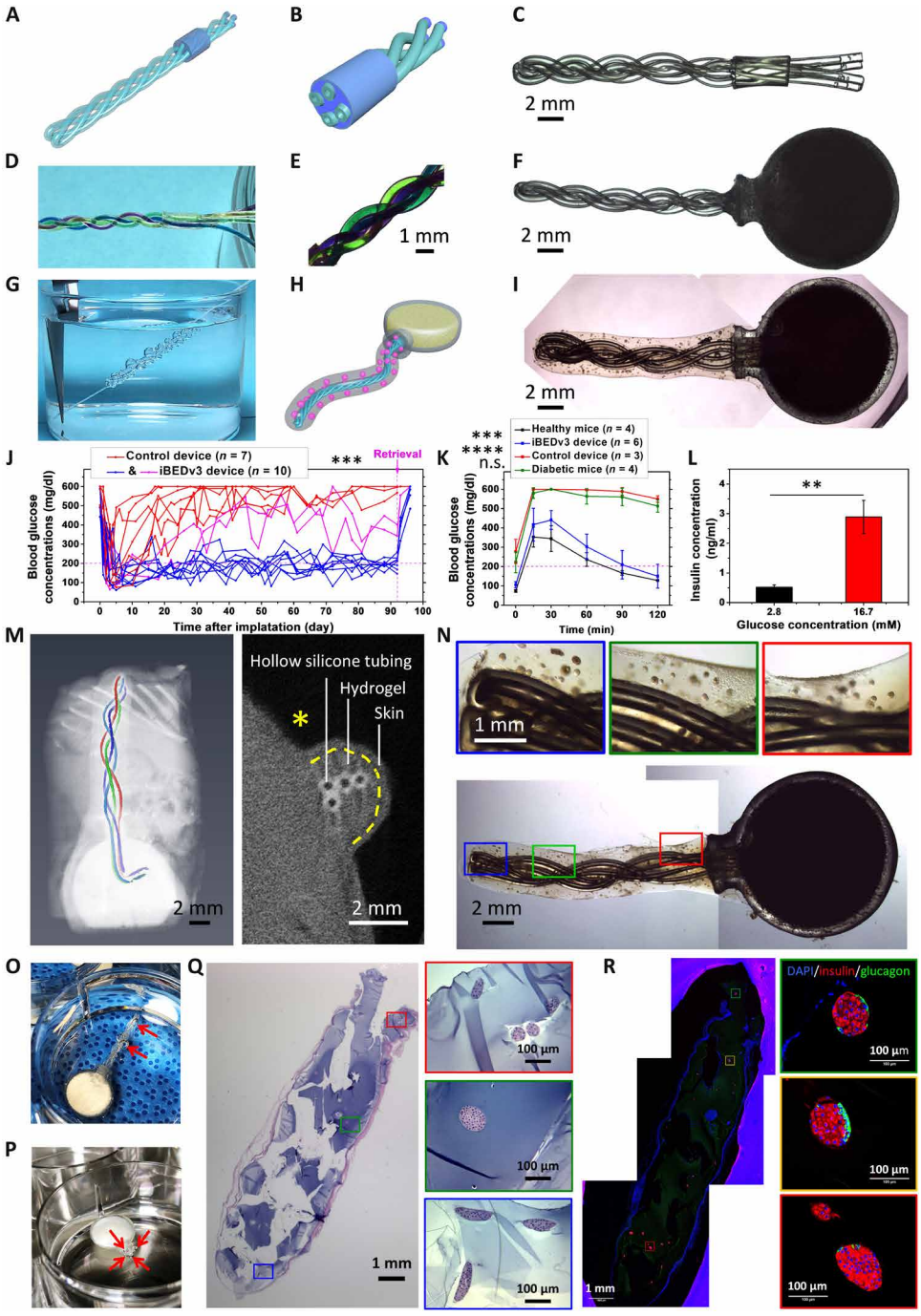


**Fig. 6. iBEDv3 design and 3-month diabetes correction in mice.** (**A** to **C**) Assembly of the twisted silicone tubing and PDMS adapter in iBEDv3. (**D** and **E**) Liquid perfusion test of the twisted silicone. (**F**) Stereo microscope image of an assembled iBEDv3. (**G**) Gas permeability test of the silicone tubing. (**H**) Schematic and (**I**) stereo microscope image showing the complete iBEDv3 device with the rat islet encapsulation hydrogel. (**J**) BG measurements in C57BL6/J mice following SC transplantation of iBEDv3 devices (blue and pink; $n = 10$) and control devices (red; $n = 7$) over 92 days; $^{***}P < 0.001$ (control versus all iBEDv3). (**K**) IPGTT test at 90 days; means ± SD, $^{****}P < 0.0001$ (iBEDv3 versus diabetic mice, iBEDv3 versus control device, and healthy mice versus control device) and $^{***}P < 0.001$ (iBEDv3 versus healthy mice); n.s. ($P > 0.05$; control device versus diabetic mice). (**L**) Static GSIS test of retrieved iBEDv3 devices ($n = 3$); means ± SD, $^{**}P < 0.01$. (**M**) 3D reconstruction (left) and transverse 2D cross-section (right) of micro-CT scan images of an iBEDv3 device in a mouse. (**N**) Stereo microscope images of one iBEDv3 device retrieved at 92 days. (**O** and **P**) $CO_2$ responsiveness of a retrieved iBEDv3 device incubated under 5% $CO_2$ with (O) the cell encapsulation hydrogel removed and (P) the twisted silicone tubing cut (red arrows indicate $O_2$ bubble formation). (**Q**) H&E and (**R**) immunohistochemical staining of retrieved iBEDv3 devices. Photo credits: (D, G, O, and P) Long-Hai Wang, Cornell University.

that robust islets were observed at locations proximal, intermediate, and distal from the tank (Fig. 6, Q and R), as well as in both superficial (fig. S24) and central (fig. S25) sections. On the other hand, control islets were largely fragmented and necrosed (fig. S26). These results demonstrated the improved, long-term performance of the optimized iBEDv3.

### Improved cell survival in pigs

We next pursued an exploratory large animal study involving xenotransplantation of rat islets in Göttingen minipigs (Fig. 7). The SC space of pigs is anatomically similar to that of humans (*48*); thus, this transplantation model provided the opportunity to study the potential for clinical translation. In addition, the xenogeneic transplantation may exacerbate immune cell infiltration and likewise fibrotic deposition near the device and thus worsen graft oxygenation. We thus hypothesized that enhanced $O_2$ supply was especially critical in this transplantation model. Our primary intents of this proof-of-concept investigation were to derive a clinically feasible transplantation procedure for the iBED design and to study the potential for iBED to support surviving, functional cells in large animals.

First, the iBEDv3 was modified and scaled to support higher islet payloads (iBEDv3S). The twisted silicone tubing was fixed in the adapter as previously described, although, in this design, the silicone tubing was only half-filled with PDMS before curing, providing protection from mechanical stress to alginate near the tank (Fig. 7A). In addition, the tank was enlarged to 22 mm in diameter and 8 mm in thickness, increasing the $Li_2O_2$/PFC-loading capacity 10-fold from the iBEDv3 design, and the tubing length was extended to 40 mm (Fig. 7B). Following incubation in 5% $CO_2$, bubbles with high and uniform $O_2$ content were found at all lengths of the tubing, suggesting maintained $CO_2$ responsiveness and rapid gas transfer throughout the device (Fig. 7, C and D, and fig. S27). The islet alginate encapsulation layer was added as done previously (Fig. 7E).

iBEDv3S devices, containing a subclinical dose of islets (1500 IEQ within 180 μl of alginate), were implanted in the ventral deep SC space in minipigs ($n$ = 4, including three minipigs for 1 month and one minipig for 2 months) (Fig. 7F and movie S3). For controls, similarly constructed devices without the inverse-breathing mechanism were implanted lateral to the iBEDv3S devices in two of the pigs. Following retrieval at 1 month, almost all islets in the control devices were fragmented or necrosed with observable pyknosis, karyorrhexis, and loss of nuclei and only weakly positive for insulin in certain regions (fig. S28), indicating the challenging nature of the SC space for cell survival. In contrast, within retrieved iBEDv3S at 1 month, numerous surviving islets were observed with healthy morphology at both proximal and distal locations from the terminal tank (Fig. 7G). Apoptosis, when detected, was found in a few peripheral islet cells (fig. S29, D and H), rather than in central cells, suggesting that these cells might have died from a xenogeneic immune response rather than hypoxia. Immunostaining also revealed positive expression of insulin in retrieved islets, indicating maintained islet function (Fig. 7H and fig. S29, E to H). For comparison, insulin expression was 9.6-fold higher, and DAPI content was 3.4-fold higher in islets from the iBEDv3S devices than that from the control devices (fig. S29I). Characterization of the retrieved iBEDv3S at 2 months also revealed several intact and insulin-positive islets (although a higher portion of cells, again in the islet peripheries, exhibited apoptosis) (fig. S30). These data demonstrate that the iBEDv3S was able to notably improve cell survival and function in a xenogeneic SC transplantation in large animals.

## DISCUSSION

Despite several decades of laboratory and clinical investigation, widespread clinical translation of islet encapsulation technology has not been realized, in part, due to $O_2$ limitations. Additional $O_2$ supply is critical for supporting islet survival and function and for permitting surgically realistic device volumes. Several thousand functional IEQ per patient kilogram are required to restore normoglycemia in a human patient (*49*), and in the absence of $O_2$ supplementation, they must be widely dispersed, even in thin constructs, to preserve $O_2$ availability (*12*, *40*). This results in infeasibly large estimated device sizes, on the order of meters for a cylindrical geometry, required to deliver a metabolically relevant payload (*50*). Enhanced $O_2$ supply allows islets to be encapsulated at higher densities without sacrificing $O_2$ availability, thus reducing the required graft volume to a manageable level surgically.

While several $O_2$ supplementation approaches have been reported previously, all of which have demonstrated benefit to encapsulated cells, challenges remain. For example, the βAir device (Beta-O2) provides supraphysiological $pO_2$ levels via daily injections into a gas-permeable chamber (*20*, *51*). This device, however, requires daily purging and refilling, otherwise, irreversible graft failure occurs rapidly (*20*). $O_2$ delivery by electrolysis has also been explored, although application in vivo has not yet been reported (*52*). In addition, excess hydrogen produced at the cathode diffuses into the host tissue, which may not be adequately cleared, and thus presents a potential problem at the transplantation site. The $CaO_2$-containing constructs provide $O_2$ supply via a hydrolytic chemical reaction (*27*–*29*). However, as explained earlier, water is a suboptimal reactant for in vivo $O_2$ generation.

The inverse-breathing system of the device we described here provides an alternative solution to $O_2$ supplementation that could overcome many challenges discussed above. Here, $O_2$ was produced for the cells by their own waste product, $CO_2$, which is ubiquitous in tissues and is self-regulated, unlike water. As a result, the steady, self-controlled $CO_2$ levels facilitated the continuous release of $O_2$ over several months. Further, $O_2$ production (in the terminal tank) was physically separated from the encapsulated cells, which avoided any harmful impact of the $O_2$ generation process (e.g., pH, side products, and temperature change) on the cells. We emphasize that the iBED system combined the advantages of four unique properties of its constituent materials. Beyond the benefit of $CO_2$ responsiveness, $Li_2O_2$ has the highest $O_2$ content of all inorganic peroxides [~33% (w/w) versus ~16% (w/w) for $CaO_2$, considering commercial purities] and thus can supply the highest amount of $O_2$ per unit weight. We maximized this potential by immersing the particulates in PFC, which has the distinctive capacity to resist water and dissolve high quantities of $O_2$ and $CO_2$ (*34*). Furthermore, the high-gas permeability (and solid/liquid impermeability) of silicone (*32*) and rapid gas-phase $CO_2$ and $O_2$ diffusion in air ensured rapid $O_2$ delivery despite the physical separation between the cells and the $O_2$-generating reaction (*38*, *39*). The advantages of these features contributed in concert to maximize the performance of the inverse-breathing system.

There are a few outstanding considerations concerning the clinical translation of this device. For example, while no adverse reactions were observed to the tank material in this study (fig. S11C) or

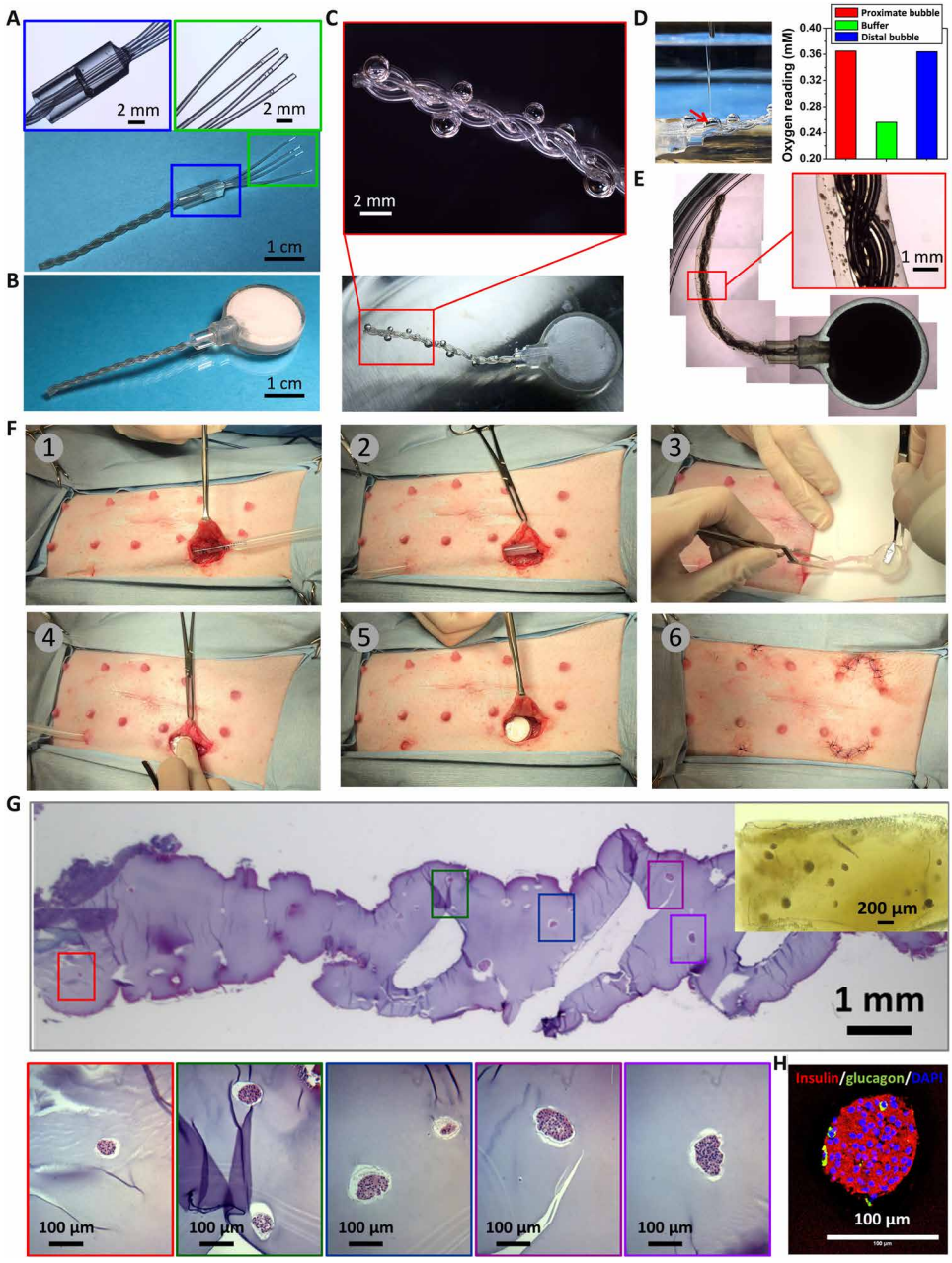


**Fig. 7. SC xenotransplantation in minipigs.** (**A** and **B**) Device assembly of iBEDv3S. (**C**) Digital and stereo microscope images showing $O_2$ bubble formation along the silicone scaffold after incubation in 5% $CO_2$ and 20% $O_2$. (**D**) $O_2$ measurement setup (left) showing the $O_2$ probe inserted into a bubble (the red arrow indicates the $O_2$ microsensor tip) and $O_2$ readings (right) in bubbles and buffer. (**E**) Stereo microscope images of the iBEDv3S device with the rat islet encapsulation hydrogel. (**F**) Surgical transplantation procedure in a Göttingen minipig: (1) Two incisions were made and connected by a pipet through the deep SC space as a guide wire; (2) a hollow silicone tube was fed along the pipet through the incisions, and the pipet was withdrawn; (3) the device was inserted into the hollow silicone tube from the cell encapsulation end; (4) the tank was situated at the end of the semicircular incision in the deep SC pocket, and (5) the hollow silicone tube was pulled out through the other incision, leaving the device in the SC space; (6) both incisions were suture-closed. (**G**) H&E staining of the retrieved device at 1 month; inset: a stereo microscope image of a region of hydrogel. (**H**) Immunohistochemical staining of retrieved islets. Photo credits: (A to D and F) Long-Hai Wang, Cornell University.

in a previous work (*53*), it may not meet regulatory standards for long-term implantation in humans. However, we note that this component can be also fabricated from clinically approved materials such as titanium. The use of the printable resin in the studies here simply provided convenience necessary for prototyping. Furthermore, although the physical containment of $Li_2O_2$ would obviate concerns of their potential toxicity, the prevention of mechanical failure is critical for translation and a perfectly safe device such as the implantable biomedical pacemaker with safely isolated lithium component (*54*) should be pursued in the future.

We also acknowledge that, in the current design, $O_2$ supply in this system is finite. While only 3 g of $Li_2O_2$ are required to sustain

500,000 IEQ of human islets (a standard approximation of the dosage used in clinical islet transplantation) for over 1 month (table S1), device replacement is impractical. However, $O_2$ supply may be extended indefinitely by the introduction of a tank replacement (fig. S31A) or formulation-refilling (fig. S31B) system, of which we have several preliminary designs. There is also the question of scaling the device to support clinically relevant islet volumes. This may be accomplished by extending the tubing length (fig. S32A), implementing a multiarm design (fig. S32B), or using a silicone tubing with a larger diameter (fig. S32C). A planar prototype with multiple aeration channels connected to the terminal tank was also fabricated to this aim (fig. S32D). Last, we propose designs to increase silicone surface area within the terminal tank, such as incorporating a silicone balloon within the terminal tank, which should increase the $O_2$ production rate from the tank to support higher cell loads (fig. S32E). Future efforts will be dedicated to addressing these translational considerations.

Here, the iBED system was extensively tested in vitro and in vivo. Initially, a simple inverse-breathing construct improved cell survival in hypoxic culture in vitro and in vivo, validating the efficacy of physiological $CO_2$-regulated $O_2$ production for encapsulated cells. Thereafter, a first-generation device (iBEDv1) improved cell survival and metabolic function following SC transplantation in mice for 2 months. Following a series of model-guided design optimizations, a third-generation device (iBEDv3) achieved sustained $O_2$ supply and diabetes correction in mice for 3 months, about 10 times longer than the nonoxygenated control, following transplantation in the SC site. Last, a scaled third-generation device (iBEDv3S) was designed and implanted in the SC space of minipigs. Even in the xenogeneic environment (which may be more challenging than clinical human-to-human allotransplantation), numerous surviving and functional islets were found following retrieval at 1 and 2 months. These findings show substantial progress in the translation of in situ long-term $O_2$ supplementation systems for encapsulated islets.

In this work, the design, characterization, and testing of a novel system and device were presented to overcome limitations of $O_2$ supplementation in cell replacement therapies. Critically, $O_2$ production in iBED was regulated by $CO_2$, a waste product of the encapsulated cells and cells in the surrounding tissues. This key self-regulation feature enabled the sustained delivery of $O_2$ for several months without intervention. The inverse-breathing system presented here provides a novel solution to many problems of supplying $O_2$ to encapsulated cells and represents a self-sustaining technology well suited for realizing clinical translation of cell replacement therapies in the SC site.

## MATERIALS AND METHODS

### Chemicals

Sodium chloride (NaCl), calcium chloride dihydrate ($CaCl_2{\cdot}2H_2O$), barium chloride dihydrate ($BaCl_2{\cdot}2H_2O$), calcium sulfate dihydrate ($CaSO_4{\cdot}2H_2O$), lithium carbonate ($Li_2CO_3$), and D-glucose were purchased from Sigma-Aldrich. Lithium peroxide ($Li_2O_2$) was purchased from Alfa Aesar. PFC oil (Krytox GPL103) was purchased from DuPont. PDMS (Sylgard 184) was purchased from Dow Corning. Ultrapure sodium alginate (Pronova SLG100) was purchased from NovaMatrix. The Dental LT Clear resin and flexible resin for 3D printing were purchased from Formlabs. Water was deionized to 18.2 MΩ·cm with the Synergy Ultraviolet Purification System (Millipore Sigma).

### Animals

Eight-week-old male C57BL/6J mice were purchased from the Jackson laboratory (Bar Harbor, ME). Male Sprague-Dawley rats (weight of ~300 g) were purchased from Charles River Laboratories (Wilmington, MA). Six-month-old female Göttingen Minipigs were purchased from Marshall Bioresources (North Rose, NY). All animal procedures were approved by the Cornell Institutional Animal Care and Use Committee.

### Characterizations

H&E staining images were taken using an Aperio Scanscope (CS2). Optical and fluorescent microscope images were taken using a digital inverted microscope (EVOS FL). Stereo microscope images were taken using a stereomicroscope (Olympus SZ61). Confocal images were taken using a laser scanning confocal microscope (LSM 710). Three different Clark-type $O_2$ sensors were used for $O_2$ measurement. An $O_2$ sensor (Vernier) equipped with a wide tip (~12 mm) was used to test the $CO_2$ responsiveness of the $Li_2O_2$/PFC@silicone tubing construct (Fig. 1, C and E to G). An $O_2$ microsensor (OX-100, Unisense) equipped with a 100-μm glass tip was used to measure the $pO_2$ in the bubbles generated around the device (Fig. 7D and fig. S23). An $O_2$ needle sensor (OX-N, Unisense) equipped with a 1.1 mm by 40 mm piercing needle was used to measure the pO2 in the lumen of device (fig. S19).

### Surface roughness modification of silicone tubing by salt leaching

A two-part hollow mold with an inner diameter of 3 mm was printed on a 3D printer (Form 2, Formlabs) using a flexible resin. A thin layer of NaCl salt was placed at the bottom of each half piece, and then curable PDMS resin was applied on the top of NaCl salt. After the PDMS resin settled down and permeated through the NaCl salt layer, a silicone tubing (Specialty Manufacturing Inc., class VI; i.d., ~1.47 mm; o.d., ~1.96 mm) was placed between two half round pieces (fig. S3A). The mold was fastened and put into an oven at 60°C. After curing for 3 hours, the tubing was unmolded. The coated tubing was soaked in hot water to leach out the NaCl.

### Fabrication of different versions of iBED designs and the corresponding control devices

To fabricate the $Li_2O_2$/PFC@silicone tubing device, the silicone tubing (2 cm in length; i.d., ~1.47 mm; and o.d., ~1.96 mm) surface was modified via the salt-leaching method (described in another section). Then, the surface-roughness–modified silicone tubing was incubated in dopamine solution [2 mg/ml in 10 mM tris buffer (pH 8.5)] overnight to create a hydrophilic external polydopamine coating (*55*). Next, the lumen was filled with 20% (w/w) $Li_2O_2$/PFC [or 20% (w/w) $LiCO_3$/PFC in controls] and sealed with PDMS resin at both ends. $CaSO_4$ was then deposited onto the tubing surface by dipping the tubing in a 1% (w/v) $CaSO_4$/ethanol suspension and allowing excess ethanol to evaporate. Last, a layer (~500 μm) of ultrapure sodium alginate (Pronova SLG100) was created by filling a cylindrical mold with alginate solution and inserting the tubing into the mold; alginate crosslinking occurred by the outward radial diffusion of $Ca^{2+}$ ions from the scaffold surface. Constructs, which contained islets or cells, were fabricated by premixing the alginate solution with the desired cells before application onto the modified silicone tubing.

To fabricate iBEDv1, a reserve tank (12 mm in diameter and 4 mm in thickness) was printed on a 3D printer (Form 2, Formlabs)

using a Dental LT Clear resin. A thin layer of liquid uncured resin was then painted onto the tank and cured at 70°C under blue light (405 nm) for 20 min, providing a smoother surface and patching over any potential gaps or defects between the printed layers (fig. S9A). The tank was filled with 20% (w/w) $Li_2O_2$/PFC [or 20% (w/w) $Li_2CO_3$/PFC in control] and attached with a 1.5-cm $Li_2O_2$/PFC@silicone tubing construct (fabricated as previously described) via an adapter. The adapter was composed of an unmodified silicone tubing (4 mm in length) filled and cured with PDMS resin. To facilitate attachment to the terminal tank, a layer of PDMS resin was applied around the adapter and cured to seal the gap between adapter and tank neck. Five hundred IEQ of rat islets distributed in a layer of ~500-μm-thick alginate at a density of ~6250 IEQ/ml were incorporated in the iBEDv1.

Fabrication of iBEDv2 was identical to that of iBEDv1, with the exception that in iBEDv2, the lumen of the silicone tubing was left empty. To fabricate an iBEDv2 to support lumen pO2 measurements, an unmodified silicone tubing was attached to the reserve tank. The free end of the tubing was then capped with a half-sealed larger silicone tubing (i.d., ~3.35 mm), and the gap between two cylinders was sealed with PDMS resin (fig. S19A).

To fabricate iBEDv3, two hollow silicone tubes (i.d., ~0.34 mm; o.d., ~0.64 mm) were twisted and folded at one end and sealed at the other, creating a four-thread twisted structure resembling the simulated quadruple helix (Fig. 6A). An adapter, which connected the terminal tank to the cell encapsulation domain, was fabricated as follows: The twisted silicone hollow tubes were fit through a short, larger hollow silicone tube (4 mm in length and i.d., ~1.47 mm) and fixed into place by filling the gap among these four small tubing and the large tubing with PDMS resin. Five hundred IEQ of rat islets distributed in a layer of ~500-μm-thick alginate at a density of ~8330 IEQ/ml were incorporated in the iBEDv3.

To fabricate the scaled-up third-generation iBED design (iBEDv3S), an enlarged reserve tank (22 mm in diameter and 8 mm in thickness) was 3D printed as described previously. The length of twisted silicone tubing was extended to 40 mm. The twisted silicone tubing was fixed in a larger adapter (12 mm in length and i.d., ~3.35 mm) as described in iBEDv3. The adapter was half-filled with PDMS before curing, providing protection from mechanical stress to the alginate near the tank (Fig. 7A). One thousand five hundred IEQ of rat islets were incorporated in the iBEDv3S at a same density as in iBEDv3.

To fabricate the controls of different iBED designs, each experimental control device is identical to its corresponding iBED design, with the exception that the $Li_2O_2$/PFC filling was replaced with $Li_2CO_3$/PFC, which does not produce oxygen. All devices were sterilized using a hydrogen peroxide plasma sterilizer before the cell encapsulation procedure.

### Rat islet isolation and purification

Sprague-Dawley rats (~300 g) were used for harvesting islets. The rats were anesthetized using 3% isoflurane in $O_2$, and the anesthesia was maintained throughout the whole surgery. Briefly, the bile duct was cannulated, and the pancreas was distended with 10 ml of 0.15% Liberase (Roche) in M199 media (Gibco). The pancreas was digested at 37°C circulating water bath for ~28 min (digestion time varied slightly for different batches of Liberase). The digestion was stopped by adding cold M199 media with 10% fetal bovine serum (FBS) (Gibco). After vigorously shaking, the digested pancreases were washed twice with media (M199 and 10% FBS), filtered through a 450-μm sieve, then suspended in a Histopaque 1077 (Sigma-Aldrich)/M199 media gradient, and centrifuged at 1700 relative centrifugal force with 0 break and 0 acceleration for 17 min at 4°C. This gradient centrifugation step was repeated for higher purity. Last, the islets were collected from the gradient and further isolated by a series of gravity sedimentations in which each top supernatant was discarded after 4 min of settling. IEQ of purified islets was counted by reported IEQ conversion factors (*56*). Islets were then washed once with islet culture media (RPMI 1640 and 10% FBS and 10 mM Hepes and 1% penicillin/streptomycin) and cultured in this medium overnight before further use.

### Hypoxic cell culture

Hypoxic cell culture was performed in a New Brunswick Galaxy CO-170 incubator, which has dynamic control over $CO_2$ and $O_2$ levels. The incubator was equipped with both compressed $CO_2$ and $N_2$ gas cylinders. The CO-170 incubator controlled internal $pO_2$, when set below ambient levels, by modulating $N_2$ inflow.

### In vitro cell viability study

INS-1 cells were cultured in RPMI 1640 medium (Gibco) supplemented with 2 mM glutamine (Gibco), 1 mM sodium pyruvate (Gibco), 10 mM Hepes (Gibco), 10% FBS (Gibco), 50 μM β-mercaptoethanol (Gibco), and 1% penicillin/streptomycin (Gibco). INS-1 cells (2.5 million cells/ml) were incorporated into $Li_2O_2$/PFC@silicone constructs and $Li_2CO_3$/PFC@silicone controls and incubated in a hypoxic incubator with 1% $O_2$ and 5% $CO_2$. After 24 hours of incubation, the cells were stained with the LIVE/DEAD Viability/Cytotoxicity Kit (Invitrogen).

### Immunochemical detection of islet hypoxia

$Li_2O_2$/PFC@silicone tubing devices containing encapsulated rat islets were cultured in a hypoxic incubator with 1% $O_2$ and 5% $CO_2$. After 24 hours of incubation, pimonidazole (Hypoxyprobe) was added to the culture media at a final concentration of 200 μM, and then the samples were returned to the incubator for an additional 2 hours of incubation. The samples were then fixed in 10% formalin and were permeabilized with 0.5% Triton X-100 for 30 min at room temperature. After cells were blocked for unspecific binding in 5% donkey serum, the samples were incubated overnight at 4°C with fluorescein isothiocyanate–conjugated anti-pimonidazole mouse immunoglobulin G1 (IgG1) monoclonal antibody (1:200; Hypoxyprobe). The formation of pimonidazole-protein adducts were analyzed by a fluorescent microscope (EVOS fl) and a confocal microscope (LSM 710).

### Morphology and immunohistochemistry of islets and retrieved samples

$Li_2O_2$/PFC@silicone tubing devices containing encapsulated rat islets were cultured in a hypoxic incubator with 1% $O_2$ and 5% $CO_2$. After 24 hours of incubation, the samples were then fixed in 10% formalin, embedded in paraffin, and sectioned by Cornell's Histology Core Facility. Sections (5 μm) were stained with H&E. For immunofluorescent insulin and glucagon staining, paraffin-embedded sections were deparaffinized in xylene and sequentially rehydrated in 100% ethanol, 95% ethanol, 75% ethanol, and PBS. Slides were then boiled in citric acid buffer [10 mM citric acid and 0.05% Tween 20 (pH 6.0)] for 30 min for antigen retrieval. After blocking with 5%

donkey serum, primary rabbit anti-rat insulin (1:200; Abcam, ab63820) and mouse anti-rat glucagon (1:200; Abcam, ab10988) antibodies were applied and incubated overnight at 4°C. After washing with PBS, Alexa Fluor 594–conjugated goat anti-rabbit IgG (1:400; Thermo Fisher Scientific, A11037) and Alexa Fluor 488–conjgated donkey anti-mouse IgG (1:400; Thermo Fisher Scientific, A21202) were applied and incubated for 60 min. Last, slides were washed with PBS, applied with antifade/DAPI, and covered with glass coverslips.

Samples retrieved from animals were fixed in 10% formalin, embedded in paraffin, and sectioned by Cornell's Histology Core Facility. Sections (5 μm) were stained with H&E. Insulin and glucagon staining were performed as described above. α–Smooth Muscle–Cy3 (1:200; Sigma-Aldrich, C6198) was used for myofibroblast staining. Anti-mouse CD68-AF488 (1:200; BioLegend, catalog no. 137012) was used for macrophage staining. Primary antibody rabbit anti-CD3 (1:100; Abcam, ab5690) and second antibody Alexa Fluor 594–conjugated goat anti-rabbit IgG (1:400; Thermo Fisher Scientific, A11037) were used for T cell staining.

### Computational modeling

A finite element model was developed to study the impact of device design on islet oxygenation. The control, iBEDv1, and iBEDv2 geometries were analogous, featuring concentric cylinders representing the alginate, PDMS tubing, and lumen content (i.e., air in the control and iBEDv2 and PFC in iBEDv1), respectively; the iBEDv3 geometry was implemented as a cylinder, representing the alginate, and an internal quadruple helix representing the silicone tubing (i.d., ~0.34 mm; o.d., ~0.64 mm) and internal air (Fig. 4B and fig. S16). Transport in the terminal storage tank was not considered; rather, $O_2$ production was implemented at a constant rate of $3.2 \times 10^{-9}$ mol/min ($4.7 \times 10^{-6}$ mol/day), converted to a surface flux by dividing by surface area at the lumen-tank interface (fig. S17). This production rate was determined as follows: (i) iBEDv2 devices were incubated in a hypoxia incubator with 5% $O_2$ and 5% $CO_2$ for 2 weeks, and then the devices were transferred into a preequilibrated hypoxia chamber (5% $O_2$ and 5% $CO_2$; fig. S19D) to measure the lumen $pO_2$ in devices with a Clark electrode, providing values of 85 to 99 mmHg (fig. S19E); (ii) an in silico iBEDv2 model was developed that omitted the encapsulated islets, and a production rate was determined such that the model-predicted lumen $pO_2$ was on the conservative end of this range at ~90 mmHg. Note that this value is consistent with the expected $O_2$ generation rate from 50 mg of $Li_2O_2$ (the amount loaded in the iBEDv2 tank) constitutively produced over the observed period of $O_2$ generation of ~4 months. It was assumed that a constant $pO_2$ of 40 mmHg was maintained at all locations of the device-host boundary (fig. S17).

Islet size and seeding were carefully considered. Optical microscope images from three rat islet isolations ($n$ = 1660 islets) were collected, and islet perimeters were traced manually using ImageJ and converted into effective diameters ($d_{eff}$) by the area method. These were sorted by size, an exact cumulative frequency curve of $d_{eff}$ was then calculated and, lastly, fit to a lognormal cumulative distribution function; a robust fit was found with shape factor $\sigma$ = 0.36, and scale factor $m$ = 119.7 ($R^2$ = 0.998; the probability density function for a lognormal distribution is given by Eq. 3)

$$f(d_{\text{eff}}) = \frac{1}{d_{\text{eff}}\sigma\sqrt{2\pi}} \exp\left(-\frac{\ln\left(\frac{d_{\text{eff}}}{m}\right)^2}{2\sigma^2}\right) \quad (3)$$

This is comparable with distributions in other species and is consistent with theoretical models of islet growth kinetics (*56*). A total of 500 IEQ of islets with diameters selected randomly from this distribution were included in each iteration.

Oxygen concentration ($c_{O_2}$) was governed by the steady-state diffusion-reaction mass balance equation with assumed negligible convection (Eq. 4)

$$D_{O_2,i}\left(\frac{1}{r}\frac{\partial}{\partial r}\left(r\frac{\partial c_{O_2}}{\partial r}\right) + \frac{1}{r^2}\frac{\partial^2 c_{O_2}}{\partial \theta^2} + \frac{\partial^2 c_{O_2}}{\partial z^2}\right) = R_{O_2,i} \quad (4)$$

In Eq. 4, diffusivity ($D_{O_2,i}$) represents the diffusivity of $O_2$ in domain i (i.e., in silicone, PFC, air, alginate, or islets) at 37°C and were selected according to values reported in the literature: $D_{O_2,silicone} = 3.25 \times 10^{-9}$ m$^2$/s (*57*), $D_{O_2,PFC} = 5.6 \times 10^{-9}$ m$^2$/s (*38*), $D_{O_2,air} = 1.8 \times 10^{-5}$ m$^2$/s (*39*), $D_{O_2,alginate} = 2.7 \times 10^{-9}$ m$^2$/s (*58*), and $D_{O_2,islets} = 2.0 \times 10^{-9}$ m$^2$/s (*40*). Last, $R_{O_2,i}$ represents $O_2$ consumption in domain *i*. $R_{O_2,i}$ was zero in all domains except the islets, where it was implemented using Michaelis-Menten kinetics and a step-down function to simulate the lack of $O_2$ consumption in necrosed cells (Eq. 5), as in other models (*59*, *60*)

$$R_{O_2,islets} = \begin{cases} 0, & c_{O_2} < c_{necrosis} \\ \dfrac{R_{max} c_{O_2}}{c_{O_2} + K_m}, & c_{O_2} \geq c_{necrosis} \end{cases} \quad (5)$$

where $R_{max} = 0.034$ mol/(m$^3$ s) represents the maximum $O_2$ uptake rate of rat islets (*40*), $K_m = 1.0 \times 10^{-3}$ mol/m$^3$ represents the half-maximal coefficient (obtained from studies of mitochondrial respiration) (*61*), and $c_{necrosis} = 1.0 \times 10^{-4}$ mol/m$^3$ represents a viability threshold (*50*, *62*). Solving Eq. 4 for $c_{O_2}$ yields spatial $O_2$ distributions; $c_{O_2}$ was converted into $pO_2$ in presented data (Fig. 4 and fig. S18) by dividing $c_{O_2}$ by Bunsen solubility values for each respective domain or via the ideal gas law in the case of air (Eq. 6)

$$pO_2 = \frac{c_{O_2}}{\alpha_{O_2,i}} \quad (6)$$

where $\alpha_{O_2,silicone} = 7.3 \times 10^{-5}$ mol/(m$^3$ Pa) (*62*), $\alpha_{O_2,PFC} = 1.9 \times 10^{-4}$ mol/(m$^3$ Pa) (*12*, *63*), $\alpha_{O_2,air} = 3.9 \times 10^{-4}$ mol/(m$^3$ Pa), $\alpha_{O_2,alginate} = 9.3 \times 10^{-6}$ mol/(m$^3$ Pa) (*12*), and $\alpha_{O_2,islets} = 7.36 \times 10^{-6}$ mol/(m$^3$ Pa) (*12*, *40*). At all internal interfaces, a partition coefficient ($K_{i|j}$) represented by the Bunsen solubility ratios was implemented (Eq. 7)

$$K_{i|j} = \frac{\alpha_{O_2,i}}{\alpha_{O_2,j}} \quad (7)$$

Meshes were generated using the "free tetrahedral" tool in COMSOL Multiphysics 5.4 (Burlington, MA) with the following settings: maximum element size of 400 μm, minimum element size of 0.3 μm, curvature factor of 0.4, resolution of narrow regions of 1.1, and maximum element growth rate of 1.125. The fitting of the lognormal distribution parameters was performed with the Curve Fitting Toolbox in MATLAB (Natick, MA). Random size selection and seeding were also performed with MATLAB. For each design, the size and seeding of the simulated islets were rerandomized, and the results were recomputed 100 times (i.e., a Monte Carlo simulation) using the COMSOL Livelink for MATLAB software. Results in Fig. 4 (C to E and G) and fig. S18D were collected from one iteration selected at random; results in Fig. 4F and fig. S18 (A to C) were collected from the aggregate of all iterations.

### EPR $O_2$ distribution mapping

All $pO_2$ maps were obtained using a JIVA-25 instrument (O2M Technologies, LLC) at the JDRF (Juvenile Diabetes Research Foundation) supported "Oxygen Measurement Core" facility. JIVA-25 operates at 720 MHz. The trityl radical, OX063-d24 (methyl-tris[8-carboxy-2,2,6,6-tetrakis[(2-hydroxyethyl]benzo[1,2-d:4,5-d′]bis[1,3] dithiol-4-yl]-trisodium salt), was obtained from the N.N. Vorozhtsov Novosibirsk Institute of Organic Chemistry. The devices (control or iBEDv3 devices) were added to 3 ml of solution (either 1% gelatin or 100 mM $CaCl_2$ in water) in a glass tube (VWR, 15 mm by 85 mm). OX063-d24 (72 mM) was added to the solution to achieve a final concentration of 1 mM. $N_2$, $CO_2$, and mixed-gas (5% $CO_2$, 5% $O_2$, and 90% $N_2$) cylinders for these studies were purchased from Medox Inc. The gas mixture of 5% $CO_2$ and 95% $N_2$ was prepared using MC gas mass flow controllers (Alicat Scientific, model numbers MC-50SCCM-D/5M and MC-5SCCM-D/5M). Deoxygenation was achieved using 100% $N_2$ using a submerged tubing at the rate of 10 standard cubic centimeter per minute (SCCM). Dissolved gas equilibration was achieved by bubbling of gas mixture (either 5% $CO_2$ and 95% $N_2$ or 5% $CO_2$, 5% $O_2$, and 90% $N_2$) at the rate of 6 SCCM. Thereafter, gas mixture overhead flow was at the rate of 6 SCCM. Average $pO_2$ measurements of the whole system (solution and device) were performed using inversion recovery electron spin echo (IRESE) sequence with the following parameters: pulse lengths of 60 ns, eight phase cycles scheme with free induction decay (FID) suppression, spin echo delay of 500 ns, 80 logarithmically spaced delays from 350 ns to 40 μs, and 55-μs repetition time. The curves were fitted using single exponential recovery to extract spin-lattice relaxation rates $R_1$ ($1/T_1$) values that were converted to $pO_2$. The $pO_2$ calibration details are as follows: $O_2$ relaxation rate at 0 mmHg $0.115 \times 10^6$ $s^{-1}$ and the slope of $124.6 \times 10^{-6}$ mmHg/$s^{-1}$. $pO_2$ imaging was performed using IRESE sequence with the following parameters: pulse lengths of 60 ns, eight phase cycles scheme with FID suppression, spin echo delay of 500 ns, equal solid-angle spaced 654 projections, 67 baselines, gradient (1.5 G/cm), eight time delays from 350 ns to 30 μs, 45-μs repetition time, and overall 10-min image duration. Images were reconstructed using filtered back projection in isotropic $64 \times 64 \times 64$ cube with 0.66-mm voxel linear size.

### In vivo x-ray micro-CT imaging in mice

Micro-CT analyses were performed on the SkyScan 1276 System (Bruker). The mice were anesthetized using 3% isoflurane in oxygen, then were placed in an exchangeable animal cassette, and maintained the anesthesia throughout the whole scanning process. During the scans, the x-ray source was set to a voltage of 80 kV and a current of 200 μA. The images were obtained using a binning mode of $2 \times 2$. The resolution of the obtained images is around 20 μm per pixel. The obtained images were reconstructed into 2D transverse cross sections using NRecon software (version 1.7.4.2). Subsequently, 3D reconstruction was performed using Avizo software (version 8.1.1). A segmentation process was conducted to visualize the maintained hollow structure of the silicone tubing based on the different absorption contrasts between the gas phase and the silicone tubing, hydrogel, and mouse tissue.

### Implantation and retrieval in mice

Eight-week-old male C57BL/6J mice were used for device implantations. To create diabetic mice, healthy mice were administered an intraperitoneal injection of freshly prepared STZ (Sigma-Aldrich) solution [22.5 mg/ml in 100 mM sodium citrate buffer (pH 4.5)] at a dosage of 150 mg of STZ per kilogram of mouse. The BG levels of all mice were retested before transplantation. Only mice with nonfasted BG levels above 350 mg/dl were considered as diabetic. The diabetic mice were anesthetized with 3% isoflurane in $O_2$, and their dorsal skin was shaved and sterilized using betadine and 70% ethanol.

A lateral transverse incision (0.5 cm for a tubing device and 1.2 cm for a device featured a terminal tank) was made on the dorsum. A pocket (0.5 cm by 2.5 cm for a tubing construct and 1.2 cm by 3 cm for a device featured a terminal tank) was created in the SC space using a blunt surgical tool. The tubing device was inserted into the pocket, and the incision was closed using a nylon suture. Reflex wound clips (Roboz) were applied in certain cases when deemed necessary.

For retrieval, some devices were excised along with the surrounding skin and fibrotic capsule. For the retrieval of other devices, a 1-cm incision was made along the implanted device, and the devices were pulled out after cutting open the surround fibrotic capsule. The incision was closed using 5-0 absorbable polydioxanone (PDS II) sutures.

### Implantation and retrieval in Göttingen minipigs

Each animal received two implants in the ventral deep SC space. Two subjects received one iBEDv3S and one control device (i.e., the device without the inverse-breathing feature) with retrieval at 1 month, one received two iBEDv3S devices with retrieval also at 1 month, and one received two iBEDv3S devices with retrieval at 2 months.

The minipigs were premedicated with glycopyrrolate and butorphanol, induced with propofol, and anesthetized with isoflurane in $O_2$. The ventral skin of the minipig was shaved and prepared for sterile surgery. A 3-cm-diameter semicircular incision was made using a scalpel, and a deep SC pocket was created for the terminal tank of iBEDv3S. Another 1-cm-long transverse incision was made roughly 10 cm away from the semicircular incision. A pipet was inserted through the deep SC space connecting the two incisions acting as a guide wire. Subsequently, a hollow silicone tube featuring an inner diameter larger than the diameter of the device was fed along the guide wire from the semicircular incision. The guide wire was then withdrawn, and the cell encapsulation unit (i.e., the silicone tubing and attached rat islet encapsulation hydrogel) of the device was inserted into the lumen of the hollow silicone tube. The hollow silicone tube was then pulled out through the transverse incision, leaving the device situated within the SC space. Last, the SC tissue around the tank was sutured using 3-0 polyglactin 910 sutures, and then the skin was closed using 3-0 nylon sutures.

For retrieval, a 3-cm incision was made along the tank, and the devices were pulled out after cutting open the surround fibrotic capsule. The SC tissue was sutured using 3-0 polyglactin 910 sutures, and then the skin incision was closed using 3-0 nylon sutures.

### BG monitoring and IPGTTs

Mouse BG levels were measured by a commercial glucometer (Contour Next EZ, Bayer) with a drop of blood collected from tail vein. For the IPGTT, mice were fasted for 16 hours and administered an intraperitoneal injection of 20% glucose solution (2 g of glucose per kilogram of mouse). BG levels were measured at 0, 15, 30, 60, 90, and 120 min (an additional recording at 180 min was made for iBEDv1) following glucose injection.

### Ex vivo static GSIS assay

Krebs Ringer Bicarbonate (KRB) buffer was prepared as follows: 2.6 mM $CaCl_2{\cdot}2H_2O$, 1.2 mM $MgSO_4{\cdot}7H_2O$, 1.2 mM $KH_2PO_4$, 4.9 mM KCl, 98.5 mM NaCl, and 25.9 mM $NaHCO_3$ (all from Sigma-Aldrich) supplemented with 20 mM Hepes (Gibco) and 0.1% bovine serum albumin (Sigma-Aldrich). The retrieved devices (without the surrounding tissue) were incubated in KRB buffer supplemented with 2.8 mM glucose for 2 hours at 37°C and 5% $CO_2$. Devices were transferred and incubated in KRB buffer supplemented with 2.8 mM and then 16.7 mM glucose for 75 min each. The buffer was collected after each incubation step, and insulin concentration was measured using an ultrasensitive rat insulin enzyme-linked immunosorbent assay kit (ALPCO).

### Statistics

Results are expressed as raw data or means ± SD. For random BG measurements (Figs. 2J, 3E, and 6J), a one-way analysis of covariance (ANCOVA) was performed for measurements between day 2 and the day of device retrieval, where treatment condition (i.e., iBED-treated mice versus control-treated mice) was considered as an independent variables and time was considered a continuous covariate. Inclusion or omission of the failed devices in the iBED-treated group did not change the significance conclusion for the analysis of data in both Figs. 3E and 6J. For Figs. 3E and 6J, the data were reanalyzed via a two-way analysis of variance (ANOVA) followed by a Tukey's post hoc *P* value adjustment, where three treatment groups (iBED-treated mice and control-treated mice) were considered independent variables, and time, in this case, was considered a discrete factor to test for differences between treatment groups. This analysis also did not change the significance conclusion for these data. For the IPGTT tests (Figs. 3F and 6K), data were analyzed via a two-way ANOVA followed by a Tukey's post hoc *P* value adjustment, where treatment (i.e., healthy mice, diabetic mice, control-treated mice, and iBED-treated mice) was considered as an independent variable and time was considered a discrete factor. For the GSIS test (Fig. 6L), data were analyzed via a one-tailed paired Student's *t* test. Statistical significance was concluded at $P < 0.05$. All statistical analyses were performed in R software.

## SUPPLEMENTARY MATERIALS

Supplementary material for this article is available at http://advances.sciencemag.org/cgi/content/full/7/20/eabd5835/DC1

View/request a protocol for this paper from *Bio-protocol*.

## REFERENCES AND NOTES


1. A. U. Ernst, L.-H. Wang, M. Ma, Islet encapsulation. *J. Mater. Chem. B* **6**, 6705–6722 (2018).
2. D. W. Scharp, P. Marchetti, Encapsulated islets for diabetes therapy: History, current progress, and critical issues requiring solution. *Adv. Drug Deliv. Rev.* **67**, 35–73 (2014).
3. M.-K. Lee, Y. H. Bae, Cell transplantation for endocrine disorders. *Adv. Drug Delv. Rev.* **42**, 103–120 (2000).
4. M. A. Atkinson, G. S. Eisenbarth, A. W. Michels, Type 1 diabetes. *Lancet* **383**, 69–82 (2014).
5. C. K. Colton, Oxygen supply to encapsulated therapeutic cells. *Adv. Drug Deliv. Rev.* **67**, 93–110 (2014).
6. J. D. Weaver, D. M. Headen, M. D. Hunckler, M. M. Coronel, C. L. Stabler, A. J. García, Design of a vascularized synthetic poly (ethylene glycol) macroencapsulation device for islet transplantation. *Biomaterials* **172**, 54–65 (2018).
7. D. T. Bowers, W. Song, L.-H. Wang, M. Ma, Engineering the vasculature for islet transplantation. *Acta Biomater.* **95**, 131–151 (2019).
8. P.-O. Carlsson, F. Palm, A. Andersson, P. Liss, Markedly decreased oxygen tension in transplanted rat pancreatic islets irrespective of the implantation site. *Diabetes* **50**, 489–495 (2001).
9. A. Carreau, B. E. Hafny-Rahbi, A. Matejuk, C. Grillon, C. Kieda, Why is the partial oxygen pressure of human tissues a crucial parameter? Small molecules and hypoxia. *J. Cell. Mol. Med.* **15**, 1239–1253 (2011).
10. M. A. Bochenek, O. Veiseh, A. J. Vegas, J. J. McGarrigle, M. Qi, E. Marchese, M. Omami, J. C. Doloff, J. Mendoza-Elias, M. Nourmohammadzadeh, A. Khan, C.-C. Yeh, Y. Xing, D. Isa, S. Ghani, J. Li, C. Landry, A. R. Bader, K. Olejnik, M. Chen, J. Hollister-Lock, Y. Wang, D. L. Greiner, G. C. Weir, B. L. Strand, A. M. A. Rokstad, I. Lacik, R. Langer, D. G. Anderson, J. Oberholzer, Alginate encapsulation as long-term immune protection of allogeneic pancreatic islet cells transplanted into the omental bursa of macaques. *Nat. Biomed. Eng.* **2**, 810–821 (2018).
11. S. J. Moore, B. L. Gala-Lopez, A. R. Pepper, R. L. Pawlick, A. J. Shapiro, Bioengineered stem cells as an alternative for islet cell transplantation. *World J. Transplant.* **5**, 1–10 (2015).
12. A. S. Lewis, Eliminating oxygen supply limitations for transplanted microencapsulated islets in the treatment of type 1 diabetes, thesis, (Massachusetts Institute of Technology, 2008).
13. A. E. Vlahos, M. V. Sefton, Muted fibrosis from protected islets. *Nat. Biomed. Eng.* **2**, 791–792 (2018).
14. M. Kastellorizios, N. Tipnis, D. J. Burgess, Foreign body reaction to subcutaneous implants, in *Immune Responses to Biosurfaces* (Springer, 2015), pp. 93–108.
15. E. S. Avgoustiniatos, Oxygen diffusion limitations in pancreatic islet culture and immunoisolation, thesis, (Massachusetts Institue of Technologuy, 2003).
16. W. Moritz, F. Meier, D. Stroka, M. Giuliani, P. Kugelmeier, P. C. Nett, R. Lehmann, D. Candinas, M. Gassmann, M. Weber, Apoptosis in hypoxic human pancreatic islets correlates with HIF-1α expression. *FASEB J.* **16**, 745–747 (2002).
17. M. Sachet, Y. Y. Liang, R. Oehler, The immune response to secondary necrotic cells. *Apoptosis* **22**, 1189–1204 (2017).
18. P. de Vos, H. A. Lazarjani, D. Poncelet, M. M. Faas, Polymers in cell encapsulation from an enveloped cell perspective. *Adv. Drug Deliv. Rev.* **67**, 15–34 (2014).
19. E. S. Avgoustiniatos, C. K. Colton, Effect of external oxygen mass transfer resistances on viability of immunoisolated tissue. *Ann. N. Y. Acad. Sci.* **831**, 145–166 (1997).
20. U. Barkai, G. C. Weir, C. K. Colton, B. Ludwig, S. R. Bornstein, M. D. Brendel, T. Neufeld, C. Bremer, A. Leon, Y. Evron, K. Yavriyants, D. Azarov, B. Zimermann, S. Maimon, N. Shabtay, M. Balyura, T. Rozenshtein, P. Vardi, K. Bloch, P. de Vos, A. Rotem, Enhanced oxygen supply improves islet viability in a new bioartificial pancreas. *Cell Transplant.* **22**, 1463–1476 (2013).
21. B. Ludwig, B. Zimerman, A. Steffen, K. Yavriants, D. Azarov, A. Reichel, P. Vardi, T. German, N. Shabtay, A. Rotem, Y. Evron, T. Neufeld, S. Mimon, S. Ludwig, M. D. Brendel, S. R. Bornstein, U. Barkai, A novel device for islet transplantation providing immune protection and oxygen supply. *Horm. Metab. Res.* **42**, 918–922 (2010).
22. T. Neufeld, B. Ludwig, U. Barkai, G. C. Weir, C. K. Colton, Y. Evron, M. Balyura, K. Yavriyants, B. Zimermann, D. Azarov, S. Maimon, N. Shabtay, T. Rozenshtein, D. Lorber, A. Steffen, U. Willenz, K. Bloch, P. Vardi, R. Taube, P. de Vos, E. C. Lewis, S. R. Bornstein, A. Rotem, The efficacy of an immunoisolating membrane system for islet xenotransplantation in minipigs. *PLOS ONE* **8**, e70150 (2013).
23. B. Ludwig, S. Ludwig, A. Steffen, Y. Knauf, B. Zimerman, S. Heinke, S. Lehmann, U. Schubert, J. Schmid, M. Bleyer, U. Schönmann, C. K. Colton, E. Bonifacio, M. Solimena, A. Reichel, A. V. Schally, A. Rotem, U. Barkai, H. Grinberg-Rashi, F.-J. Kaup, Y. Avni, P. Jones, S. R. Bornstein, Favorable outcome of experimental islet xenotransplantation without immunosuppression in a nonhuman primate model of diabetes. *Proc. Natl. Acad. Sci. U.S.A.* **114**, 11745–11750 (2017).
24. B. Ludwig, A. Reichel, A. Steffen, B. Zimerman, A. V. Schally, N. L. Block, C. K. Colton, S. Ludwig, S. Kersting, E. Bonifacio, M. Solimena, Z. Gendler, A. Rotem, U. Barkai, S. R. Bornstein, Transplantation of human islets without immunosuppression. *Proc. Natl. Acad. Sci. U.S.A.* **110**, 19054–19058 (2013).
25. M. Gholipourmalekabadi, S. Zhao, B. S. Harrison, M. Mozafari, A. M. Seifalian, Oxygen-generating biomaterials: A new, viable paradigm for tissue engineering? *Trends Biotechnol.* **34**, 1010–1021 (2016).
26. B. S. Harrison, D. Eberli, S. J. Lee, A. Atala, J. J. Yoo, Oxygen producing biomaterials for tissue regeneration. *Biomaterials* **28**, 4628–4634 (2007).
27. S. H. Oh, C. L. Ward, A. Atala, J. J. Yoo, B. S. Harrison, Oxygen generating scaffolds for enhancing engineered tissue survival. *Biomaterials* **30**, 757–762 (2009).
28. E. Pedraza, M. M. Coronel, C. A. Fraker, C. Ricordi, C. L. Stabler, Preventing hypoxia-induced cell death in beta cells and islets via hydrolytically activated, oxygen-generating biomaterials. *Proc. Natl. Acad. Sci. U.S.A.* **109**, 4245–4250 (2012).
29. M. M. Coronel, J.-P. Liang, Y. Li, C. L. Stabler, Oxygen generating biomaterial improves the function and efficacy of beta cells within a macroencapsulation device. *Biomaterials* **210**, 1–11 (2019).
30. I. F. Tannock, Oxygen diffusion and the distribution of cellular radiosensitivity in tumours. *Br. J. Radiol.* **45**, 515–524 (1972).

31. E. H. Cole, J. Logothetopoulos, Glucose oxidation (14-CO2 production) and insulin secretion by pancreatic islets isolated from hyperglycemic and normoglycemic rats. *Diabetes* **23**, 469–473 (1974).
32. T. C. Merkel, V. I. Bondar, K. Nagai, B. D. Freeman, I. Pinnau, Gas sorption, diffusion, and permeation in poly(dimethylsiloxane). *J Polym Sci B* **38**, 415–434 (2000).
33. J. N. Lee, C. Park, G. M. Whitesides, Solvent compatibility of poly (dimethylsiloxane)-based microfluidic devices. *Anal. Chem.* **75**, 6544–6554 (2003).
34. J. G. Riess, Fluorocarbon-based in vivo oxygen transport and delivery systems. *Vox Sang.* **61**, 225–239 (1991).
35. *Chemistry of the* Elements, N.N. Greenwood and A. Earnshaw, Eds. (Elsevier Ltd., ed. 2, 1997).
36. P. de Vos, M. M. Faas, B. Strand, R. Calafiore, Alginate-based microcapsules for immunoisolation of pancreatic islets. *Biomaterials* **27**, 5603–5617 (2006).
37. A. Najdahmadi, A. M. Smink, P. de Vos, J. R. Lakey, E. Botvinick, Non-invasive monitoring of oxygen tension and oxygen transport inside subcutaneous devices after H2S treatment. *Cell Transplant.* **29**, 0963689719893936 (2020).
38. R. N. O'Brien, A. J. Langlais, W. D. Seufert, Diffusion coefficients of respiratory gases in a perfluorocarbon liquid. *Science* **217**, 153–155 (1982).
39. S. Chapman, T. G. Cowling, D. Burnett, *The Mathematical Theory of Non-Uniform Gases: An Account of the Kinetic Theory of Viscosity, Thermal Conduction and Diffusion in Gases* (Cambridge Univ. Press, 1990).
40. E. S. Avgoustiniatos, K. E. Dionne, D. F. Wilson, M. L. Yarmush, C. K. Colton, Measurements of the effective diffusion coefficient of oxygen in pancreatic islets. *Ind. Eng. Chem. Res.* **46**, 6157–6163 (2007).
41. K. E. Dionne, C. K. Colton, M. Lyarmush, Effect of hypoxia on insulin secretion by isolated rat and canine islets of Langerhans. *Diabetes* **42**, 12–21 (1993).
42. M. Kotecha, B. Epel, S. Ravindran, D. Dorcemus, S. Nukavarapu, H. Halpern, Noninvasive absolute electron paramagnetic resonance oxygen imaging for the assessment of tissue graft oxygenation. *Tissue Eng. Part C Methods* **24**, 14–19 (2018).
43. B. Epel, M. Kotecha, H. J. Halpern, In vivo preclinical cancer and tissue engineering applications of absolute oxygen imaging using pulse EPR. *J. Magn. Reson.* **280**, 149–157 (2017).
44. B. Epel, H. J. Halpern, In vivo pO2 imaging of tumors: Oxymetry with very low-frequency electron paramagnetic resonance, in *Methods Enzymol* (Elsevier, 2015), vol. 564, pp. 501–527.
45. A. A. Kuzhelev, D. V. Trukhin, O. A. Krumkacheva, R. K. Strizhakov, O. Y. Rogozhnikova, T. I. Troitskaya, M. V. Fedin, V. M. Tormyshev, E. G. Bagryanskaya, Room-temperature electron spin relaxation of triarylmethyl radicals at the X- and Q- bands. *J. Phys. Chem. B* **119**, 13630–13640 (2015).
46. D. An, A. Chiu, J. A. Flanders, W. Song, D. Shou, Y.-C. Lu, L. G. Grunnet, L. Winkel, C. Ingvorsen, N. S. Christophersen, J. J. Fels, F. W. Sand, Y. Ji, L. Qi, Y. Pardo, D. Luo, M. Silberstein, J. Fan, M. Ma, Designing a retrievable and scalable cell encapsulation device for potential treatment of type 1 diabetes. *Proc. Natl. Acad. Sci. U.S.A.* **115**, E263–E272 (2018).
47. A. U. Ernst, L. H. Wang, M. Ma, Interconnected toroidal hydrogels for islet encapsulation. *Adv. Healthc. Mater.* **8**, 1900423 (2019).
48. Y. Zheng, D. B. Tesar, L. Benincosa, H. Birnböck, C. A. Boswell, D. Bumbaca, K. J. Cowan, D. M. Danilenko, A. L. Daugherty, P. J. Fielder, *MAbs* (Taylor & Francis, 2012), vol. 4, pp. 243–255.
49. K. K. Papas, C. K. Colton, A. Qipo, H. Wu, R. A. Nelson, B. J. Hering, G. C. Weir, M. Koulmanda, Prediction of marginal mass required for successful islet transplantation. *J. Invest. Surg.* **23**, 28–34 (2010).
50. J. L. Dulong, C. Legallais, A theoretical study of oxygen transfer including cell necrosis for the design of a bioartificial pancreas. *Biotechnol. Bioeng.* **96**, 990–998 (2007).
51. P. O. Carlsson, D. Espes, A. Sedigh, A. Rotem, B. Zimerman, H. Grinberg, T. Goldman, U. Barkai, Y. Avni, G. T. Westermark, L. Carlbom, H. Ahlström, O. Eriksson, J. Olerud, O. Korsgren, Transplantation of macroencapsulated human islets within the bioartificial pancreas βAir to patients with type 1 diabetes mellitus. *Am. J. Transplant.* **18**, 1735–1744 (2018).
52. H. Wu, E. S. Avgoustiniatos, L. Swette, S. BONNER-WEIR, G. C. Weir, C. K. Colton, In situ electrochemical oxygen generation with an immunoisolation device. *Ann. N. Y. Acad. Sci.* **875**, 105–125 (1999).
53. D. An, L. H. Wang, A. U. Ernst, A. Chiu, Y. C. Lu, J. A. Flanders, A. K. Datta, M. Ma, An atmosphere-breathing refillable biphasic device for cell replacement therapy. *Adv. Mater.* **31**, 1905135 (2019).
54. S. K. Mulpuru, M. Madhavan, C. J. McLeod, Y.-M. Cha, P. A. Friedman, Cardiac pacemakers: function, troubleshooting, and management: Part 1 of a 2-part series. *J. Am. Coll. Cardiol.* **69**, 189–210 (2017).
55. H. Lee, S. M. Dellatore, W. M. Miller, P. B. Messersmith, Mussel-inspired surface chemistry for multifunctional coatings. *Science* **318**, 426–430 (2007).
56. P. Buchwald, X. Wang, A. Khan, A. Bernal, C. Fraker, L. Inverardi, C. Ricordi, Quantitative assessment of islet cell products: estimating the accuracy of the existing protocol and accounting for islet size distribution. *Cell Transplant.* **18**, 1223–1235 (2009).
57. D. A. Markov, E. M. Lillie, S. P. Garbett, L. J. McCawley, Variation in diffusion of gases through PDMS due to plasma surface treatment and storage conditions. *Biomed. Microdevices* **16**, 91–96 (2014).
58. Ü. Mehmetoglu, S. Ateş, R. Berber, Oxygen diffusivity in calcium alginate gel beads containing Gluconobacter suboxydans. *Artif. Cells Blood Substit. Immobil. Biotechnol.* **24**, 91–106 (1996).
59. P. Buchwald, A. Tamayo-Garcia, V. Manzoli, A. A. Tomei, C. L. Stabler, Glucose-stimulated insulin release: Parallel perifusion studies of free and hydrogel encapsulated human pancreatic islets. *Biotechnol. Bioeng.* **115**, 232–245 (2018).
60. T. M. Suszynski, E. S. Avgoustiniatos, K. K. Papas, Oxygenation of the intraportally transplanted pancreatic islet. *J. Diabetes Res.* **2016**, 1–12 (2016).
61. D. F. Wilson, W. L. Rumsey, T. J. Green, J. M. Vanderkooi, The oxygen dependence of mitochondrial oxidative phosphorylation measured by a new optical method for measuring oxygen concentration. *J. Biol. Chem.* **263**, 2712–2718 (1988).
62. W. Wijaranakula, Solubility of interstitial oxygen in silicon. *Appl. Phys. Lett.* **59**, 1185–1187 (1991).
63. M. K. Tham, R. D. Walker Jr., J. H. Modell, Diffusion coefficients of molecular oxygen, molecular nitrogen, and carbon dioxide in fluorinated ethers. *J. Chem. Eng. Data* **18**, 411–412 (1973).


**Acknowledgments:** We thank Cornell University Animal Health Diagnostic Center for histological sectioning and staining. We thank T. Porri and the BRC Imaging Facility at Cornell's Institute of Biotechnology for micro-CT analysis. **Funding:** This work was partially supported by the NIH (1R01DK105967-01A1), the Novo Nordisk Company, the Hartwell Foundation, and the Juvenile Diabetes Research Foundation (JDRF, 2-SRA-2018-472-S-B). This material is also based on work supported by the NSF Graduate Research Fellowship under grant number DGE-1650441. O2M Technologies acknowledges the support of JDRF grant 3-SRA-2020-883-M-B, NIH/NCI SBIR grants R43CA224840 and R44CA224840, and NSF SBIR grant 1819583.
**Author contributions:** L.-H.W. and M.M. conceived and designed the experiments. L.-H.W. and A.U.E. performed the experiments and data analysis. A.U.E. and A.K.D. performed the computational modeling. J.A.F., L.-H.W., and W.L. performed the minipig experiments. B.E., and M.K. contributed to the EPR $O_2$ imaging. X.W. performed some staining experiments. K.K.P. contributed to the analysis of device capacity and discussion of translation. A.U.E., L.-H.W., and M.M. wrote the manuscript. **Competing interests:** B.E. discloses financial interests in O2M Technologies. K.K.P. is a co-founder and stakeholder with management and advisory roles in Procyon Technologies LLC. L.-H.W., A.U.E., J.A.F, and M.M. are inventors on a patent based on this work filed by Cornell University (no. US 63/123,307, filed on 9 December 2020). All other authors declare that they have no other competing interests. **Data and materials availability:** All data needed to evaluate the conclusions in the paper are present in the paper and/or the Supplementary Materials. Additional data related to this paper may be requested from the authors.

Submitted 30 June 2020
Accepted 25 March 2021
Published 14 May 2021
10.1126/sciadv.abd5835

**Citation:** L.-H. Wang, A. U. Ernst, J. A. Flanders, W. Liu, X. Wang, A. K. Datta, B. Epel, M. Kotecha, K. K. Papas, M. Ma, An inverse-breathing encapsulation system for cell delivery. *Sci. Adv.* **7**, eabd5835 (2021).